Assimilation of snow water equivalent from AMSR2 and IMS satellite data utilizing the local ensemble transform Kalman filter

Joonlee lee[1], Myong-In Lee[1]*, Sunlae Tak[1], Eunkyo Seo[2,3], and Yong-Keun Lee[4]

[1] *Department of Civil, Urban, Earth, and Environmental Engineering, Ulsan National Institute of Science and Technology, Ulsan, Korea*

[2] *Department of Environmental Atmospheric Sciences, Pukyong National University, Busan, South Korea.*

[3]*Center for Ocean-Land-Atmosphere Studies, George Mason University, Fairfax, VA, USA*

[4] *Earth System Science Interdisciplinary Center, University of Maryland, College Park, U.S.A.*

~~29 July~~20 SEP 2024

To be submitted to GMD

---

*Corresponding author: Prof. Myong-In Lee, Department of Urban and Environmental Engineering, Ulsan National Institute of Science and Technology, 50 UNIST-gil, Ulsan 44919, Republic of Korea (milee@unist.ac.kr)

Abstract

Snow Water Equivalent (SWE), as one of the land initial or boundary conditions, plays a crucial role in global or regional energy and water balance, thereby exerting a considerable impact on seasonal and sub-seasonal scale predictions owing to its enduring ~~memory~~persistence over 1 to 2 months. Despite its importance, most SWE initialization remains challenging due to its reliance on simple approaches based on spatially limited observations. Therefore, this study developed the advanced SWE data assimilation framework with satellite remote-sensing data utilizing the local ensemble transform Kalman filter (LETKF) and the Joint U.K. Land Environment Simulator (JULES) land model. This approach constitutes an objective method that optimally combines two previously unattempted incomplete data sources: the satellite SWE retrieval from the Advanced Microwave Scanning Radiometer 2 (AMSR2) and dynamically-balanced SWE from the JULES land surface model. In this framework, an algorithm is additionally considered to determine the assimilation process based on the presence or absence of snow cover from the Interactive Multisensor Snow and Ice Mapping System (IMS) satellite, renowned for its superior reliability.

The baseline model simulation from JULES without satellite data assimilation shows better performance in high-latitude regions with heavy snow accumulation but relatively inferior in the transition regions with less snow and high spatial and temporal variation. Contrastingly, the AMSR2 satellite data exhibit better performance in the transition regions but poorer in the high latitudes, presumably due to the limitation of the satellite data in the penetrating depth. The data assimilation (DA) demonstrates the positive impacts by reducing uncertainty in the JULES model simulations in most areas, particularly in the mid-latitude transition regions. In the transition regions, the model background errors from the ensemble runs are significantly larger than the observation errors, emphasizing great uncertainty in the model simulations. The results of this study highlight the beneficial impact of data assimilation by effectively combining both

land surface model and satellite-derived data according to their relative uncertainty, thereby controlling not only transitional regions but also the regions with heavy snow accumulation that are difficult to detect by satellite.

1. Introduction

Snow plays a crucial role in regulating the water, energy, and carbon exchange between the land surface and atmosphere (e.g., Dutra et al., 2011; Thomas et al., 2016). A snowpack tends to increase surface albedo and soil moisture as the snow melts (Eagleson,1970), thereby affecting the climate system through changes in water and energy balances. In addition to local impacts, the continental snowpack over Eurasia can influence the large scale atmospheric circulation during winter (e.g., Li and Wang, 2014) or in spring (e.g., Broxton et al., 2017). Especially, the Eurasian autumn snow can affect upward-propagating stationary Rossby-wave activity, leading to stratospheric warming and weakening of stratospheric polar vortex and jet stream, which in turn emerges as a negative Arctic oscillation (AO)-like pattern at the surface during winter due to downward propagation through the troposphere. Its impact is shown in both observation and model experiments (e.g., Allen and Zender 2011; Cohen et al. 2007). Furthermore, the interannual variability of snow melting during the boreal spring season affects surface soil moisture in summer, which has important implications for heatwave development and emphasizing mechanisms through land-atmosphere interactions (Seo et al., 2020).

In the subseasonal to seasonal (S2S) timescales, land initial states are crucial components in the S2S timescale predictions due to the inherent memory that changes slowly for 1 to 2 months in the climate system (e.g., Derome et al. 2005; Chen et al., 2010; Seo et al., 2019). In particular, the realistic snow initial states contribute to improving S2S prediction skills, as proven in several modeling studies. For example, previous studies (Orsolini et al., 2013; Jeong et al., 2013) demonstrated a considerable enhancement in prediction skill of 2m air temperature up to a lead time of 1-2 months across certain regions of Eurasia and the Arctic during winter, depending on snow initialization. Moreover, other studies (Orsolini et al., 2016; Li et al., 2019) have revealed that wave activity propagating toward the stratosphere, influenced by snow initial conditions in climate models, can induce changes in the polar vortex and contribute to

78 the persistence of the North Atlantic Oscillation (NAO) and the AO. This emphasizes the
79 significance of snow initialization in climate models as an essential process for enhancing
80 prediction performance at the S2S timescales.

81 Snow states, i.e., snow water equivalent (SWE) used directly for hydrological analysis and
82 initial states of the model (Li et al., 2019; Gan et al., 2021), are generally provided from in-situ
83 observations data, remote-sensing retrievals from satellites, or numerical models such as the
84 land surface model (LSM) operated based on the observed atmospheric variables. For the in-
85 situ data snow depth (SD) measurements prevail, largely attributed to the challenges associated
86 with acquiring precise SWE data (Takala et al., 2011; De Rosnay et al., 2014). Surface synoptic
87 observations (SYNOP) serve as the principal source for SD measurements. The in-situ
88 measurements offer the most dependable snow information, yet they are characterized by
89 relatively coarse temporal and spatial resolutions, particularly within limited areas, due to the
90 spatial heterogeneity inherent in snow distribution. (Helmert et al., 2018; Meyal et al., 2020).
91 Satellite-derived observations using conical scanning microwave instruments may provide
92 spatially consistent data coverage across the globe. Cho et al. (2017) showed the SWE retrieval
93 results from two passive microwave sensors, the advanced microwave scanning radiometer 2
94 (AMSR2) and the special sensor microwave imager sounder (SSMIS). However, the
95 algorithms for SWE retrieval exhibit a degree of sensitivity to a variety of parameters such as
96 snow liquid water content and snow grain size distribution (De Rosnay et al., 2014). Hence,
97 satellite-based SWE data still have limitations in accuracy, especially under deep snow
98 conditions due to the limited penetration depth (Gan et al., 2021). On the other hand, satellite
99 retrieval can estimate snow cover accurately under clear sky conditions (Brubaker et al., 2009).
100 Model simulations obtained from LSMs and simple snow models can cover complete
101 spatiotemporal resolution but involve potentially large uncertainties due to the deficiencies in
102 the physical parameterizations and meteorological forcing data (Dirmeyer et al., 2006; Seo et

al., 2021).

Considering that snow observation dataset has its respective strengths as well as limitations, data assimilation or other data fusion methods can prove to be beneficial for constructing snow states such as reanalysis data (e.g., Brasnett, 1999; Dee et al., 2011; Meng et al., 2012; Pullen et al., 2011; De Rosnay et al., 2014). For example, the snow analysis for the Canadian Meteorological Center (CMC) utilizes a 2-dimensional optimal interpolation (2D-OI) scheme with in-situ observations and the outputs from a simple snow model (Brown et al., 2003). The National Centers for Environmental Prediction (NCEP) climate forecast system reanalysis (CFSR) combines a multi-satellite-based interactive multi-sensor snow and ice mapping system (IMS) as satellite-based snow cover retrieval and the outputs from the global snow model of the Air Force Weather Agency (Meng et al., 2012). At the European Center for Medium Weather Forecast (ECMWF), the ECMWF reanalysis (ERA)-Interim and ERA5 for the snow analysis employ a Cressman interpolation and 2D-OI, respectively, with the IMS, in-situ observation, and the results from a land surface model (Dee et al. 2011; De Rosnay et al., 2014). The Japanese 55-year Reanalysis (JRA55) also utilizes the 2D-OI with in-situ observation, satellite-based snow cover from SSMIS, and the results from an LSM (Kobayashi et al., 2015). Given that the majority of the reanalysis datasets rely on snow depth measurements, the SWE estimation is likely to introduce potential accuracy concerns when the snow depth information is combined with the sow density calculations.

Climate prediction systems in operational centers such as the Meteorological Office (Met Office) in the United Kingdom and the Korean Meteorological Administration (KMA) conduct the snow initialization by utilizing the results of the operational global unified model (UM) and the IMS snow cover, which solely indicates the presence of snow (Pullen et al., 2011), lacking in its ability to reflect the physical quantity of it. The initialization at NCEP also performs a similar approach using input data combined from IMS snow cover and results from the global

SD model (SNODEP; Meng et al., 2012). Furthermore, the snow initialization of ECMWF employs optimal interpolation with a combination of results from the LSM, IMS snow cover, and in-situ observation from SYNOP and national networks available on the GTS. However, in regions where ground observations are unavailable, large errors may exist in the snow model outputs due to uncertainties in atmospheric forcing and imperfect model parameterization (Boone et al., 2004; Essery et al., 2009). Often, the snow processes parameterized in LSMs rely on observed properties sampled in limited areas (Lim et al., 2022). In addition, as IMS snow cover only identifies the presence of snow, the data assimilation with the satellite snow cover only is not sufficient and inappropriate in constraining water and energy conservation. Alternative methods that consider the physical quantity of snow are required for the snow initialization.

One approach to mitigate the spatial discontinuity of ground observations is to use satellite-derived SWE with wide spatial coverage and frequent temporal resolution. However, the SWE retrievals from satellites still have considerable uncertainties (De Lannoy et al., 2010; Dawson et al., 2018), which can arise from vegetation and terrain interference, sensor signal saturation, snowfall amount, and simplifications in the underlying assumptions of the retrieval algorithms (Liu et al., 2015). In particular, a region with heavy snow accumulation leads to a significant underestimation of SWE due to the limitations in penetration depth from satellites (Gan et al., 2021), so that satellite-derived SWE is not employed in the land initialization process. In previous studies, various approaches have been attempted to improve SWE product performance, such as combining satellite-derived SWE with ground observations (Pulliainen et al., 2020), different satellite data sets (Gan et al., 2021), simple snow models (Dziubanski and Franz, 2016), or LSMs (Kwon et al., 2017; Kumar et al., 2019). However, most previous studies have focused on targeted regions with limited ground-based observations. Snow initialization in global coverage using satellite-derived SWE remains a persistently challenging

153 task.

154 Therefore, this study developed an advanced SWE data assimilation framework with satellite
155 remote-sensing data using the local ensemble transform Kalman filter (LETKF) and the Joint
156 U.K. Land Environment Simulator (JULES) land model. While there are existing studies on
157 SWE data assimilation (e.g., Oaida et al., 2019; Smyth et al., 2020; Luojus et al., 2021), the
158 use of passive microwave observations based on the LETKF in this context is relatively rare
159 (e.g., Girotto et al., 2020). This approach constitutes an objective method that optimally
160 combines two previously unattempted incomplete data sources: the satellite SWE from the
161 Advanced Microwave Scanning Radiometer 2 (AMSR2) and the dynamically-balanced SWE
162 from the JULES land model forced by observed atmospheric fields. The estimated SWE data
163 exhibit better consistence by additionally using snow cover data from the IMS data. This
164 assimilation framework also enables the assessment of improvement as it provides insights into
165 the reasons behind the performance improvement based on the Kalman gain analysis that
166 measures the relative significance of the input data between the satellite and the land model
167 during the data assimilation cycle. The satellite data have demonstrated high reliability in the
168 transition regions of climatologically-shallow snow conditions (Gan et al., 2021), and these
169 regions are known as "hot spots" of strong atmosphere-land coupling through snow melting
170 and associated surface energy and water balance changes (Koster et al., 2004; Dirmeyer, 2011;
171 Huning and AghaKouchak, 2020). From these perspectives, it would be important to evaluate
172 the impact of satellites on the transition regions as well as on the deep accumulation regions
173 where accurate satellite retrievals are challenging. Furthermore, the benefits of assimilating
174 satellite retrievals in extremely high-temperature events, such as the case in April 2020 over
175 Eurasia, can be elucidated. In this regard, we expect that this snow data assimilation framework
176 with satellite-derived SWE can be significant in providing optimal snow initial states for
177 improving the S2S prediction by global climate models.

178

2. Data and model

2.1. Satellite data

The snow information including snow cover and SWE can be derived from satellite measurements offering global coverage and high temporal as well as spatial resolution. For data assimilation, this study uses SWE calculated from brightness temperature measurements obtained by the AMSR2 on board the Japanese Aerospace Exploration Agency (JAXA) global change observation mission-water (GCOM-W) satellite. This AMSR2 Unified Level-3 (L3) dataset offers daily estimation of SWE at 25 km resolutions from July 2012 to the present. AMSR2 has a sensor designed to detect microwave radiation naturally emitted from the surface and atmosphere, employing six frequency bands ranging from 6.9 to 89 GHz. Through this conical scanning mechanism, AMSR2 can acquire day and night datasets with nearly constant spatial resolution over more than 99% of the global coverage every two days. Comprehensive explanations of AMSR2 characteristics are available in Imaoka et al. (2010). AMSR2 is selected for the assimilation because it produces more accurate results by assimilating data from modern sensors (e.g., AMSR2) compared to data from conventional sensors (e.g., AMSR-E) (Cho et al., 2017).

The widely used multisensor–derived snow cover is IMS (e.g., Ramsay 1998; Helfrich et al., 2007) produced by NOAA the National Environmental Satellite Data and Information Service (NESDIS) for the Northern Hemisphere from February 2004 to the present at 4 km resolutions. This dataset is generated using various data products, including multi-satellite images and in-situ observations (U.S. National Ice Center, 2008). Since IMS provides binary (0: no snow or 1: snow covered) snow cover information, we transform the IMS snow cover at 4 km grids to the snow cover fraction (SCF) within a 50-km LSM grid by counting the snow pixel number with a value of 1. A 50-km LSM grid is declared as snow-covered when more than 50% of the 4km pixels within the grid are covered with snow. In this study, the application

of the assimilation process is determined based on IMS-based SCF, renowned for its superior reliability (e.g., Brown et al., 2014). Further details will be described in Section 3.3.

2.2. Reference data for SWE and SCF

The CMC daily estimated SWE is used for verification. The SWE data is processed using statistical interpolation between a background field derived from a simple snow model and in-situ daily SD (Brown and Brasnett, 2010). In detail, this dataset utilizes optimal interpolation methods to acquire spatial SD from the in-situ data, involving SYNOP, special aviation reports from the World Meteorological Organization (WMO), and meteorological aviation reports (METAR). In areas with scant in-situ data, a simple snow accumulation and melt model is employed to create an optimal interpolation that estimates snowmelt and snowfall worldwide, assuming the persistence of the snowpack mass between snowfall and melting events (Brasnett, 1999). Although the average elevation of snow measurement stations used in CMC is biased toward low elevations (< 400m), potentially causing relative negative biases at higher elevations with heavy snow accumulation, the CMC dataset is often considered the premier snow analysis accessible in the Northern Hemisphere (Su et al. 2010) and has still been widely used to evaluate model outputs (e.g., Reichle et al., 2011; Reichle et al., 2017; Toure et al, 2018). Therefore, the SWE of CMC produced without the satellite-derived data is selected for verification as an independent dataset for evaluating the assimilated analysis with remote sensing snow retrievals. Since only daily SD analysis is provided in CMC, it is converted to daily SWE based on the snow bulk density methods (e.g., Sturm et al., 2010). It is available from 12 March 1998 to the present and offers comprehensive coverage of the entire Northern Hemisphere with a horizontal resolution of 24 km. The SWE of CMC at its native horizontal resolution is interpolated onto the LSM grid through local area averaging.

2.3. JULES LSM

This study utilizes the JULES LSM from the Met Office (Best et al., 2011), a component land model of the global seasonal forecasting system version 6 (GloSea6) global, fully-coupled atmosphere, ocean, land, and sea-ice model. The surface types (or snow tiles) in the JULES LSM consist of four non-vegetated types: urban, land-ice, inland water, and bare soil, as well as five vegetation functional types: C3 temperate grass, needleleaf trees, shrubs, C4 tropical grass, and broadleaf trees. For each surface tile, a separate energy balance is computed, and the average energy balance in the grid cells is determined by applying weights to the values of each surface tile. Two schemes are used within JULES to represent surface snow (e.g., Best et al., 2011; Burke et al., 2013). The simple method involves a zero-layer approach, which modifies the top soil level without using explicit model layers to represent snow processes. The other is the multi-layer approach which is more comprehensive, described in Best et al. (2011). In the case of vegetated surfaces, snow can be separated into ground snow and canopy snow or stored in a single effective reservoir. As both the zero-layer and multi-layer snow models provide similar results under various conditions (Best et al., 2011), this study used the zero-layer snow model with constant thermal conductivity and density for snow. Although the heat capacity of snow is ignored, the bulk thermal conductivity in the surface layer is reduced as the thermal conductivity of snow differs from that of the soil and the layer thickness increases. As long as snow persists on the ground, the skin temperature cannot exceed 0°C, yet the heat flux utilized for melting the snow is diagnosed as the residual in the surface energy balance. The melted water is immediately drained from the snow, divided into runoff and soil infiltration, and liquid water is not stored or frozen in the snow. A detailed description of the energy and water cycling in the JULES LSM can be referenced in Best et al. (2011).

The prognostic variables (e.g., SWE) in the LSM are determined by meteorological forcing variables such as 2-m air temperature, humidity, 10-m wind speed, precipitation, surface

pressure, and radiative fluxes. The 3-hourly, JRA55 reanalysis at 0.56° spatial resolution is employed for the meteorological forcing variables, which is linearly interpolated to a 50 km resolution of the LSM. The model background error needed for data assimilation is estimated by JULES ensemble runs with perturbed initial and boundary conditions. Following the previous studies (Reichle et al., 2008; Seo et al., 2021), meteorological forcing variables are perturbed to account for the uncertainties in these variables, especially precipitation, downward shortwave, and downward longwave. Perturbations are applied using additive adjustments assuming a normal distribution for longwave radiation and multiplicative adjustments following a log-normal distribution for shortwave radiation and precipitation, as guided by previous studies (Seo et al., 2021). Here, the ensemble means of additional and multiplicative perturbations are zero and one, respectively. The relationship between disturbed precipitation and radiative flux ensures the physical consistency among atmospheric forcing variables (Reichle et al., 2008). For instance, a negative anomaly in precipitation and downward longwave-radiation is statistically linked to a positive anomaly of downward shortwave-radiation. Detailed explanations regarding the perturbation of atmospheric forcings can be found in Reichle et al. (2008).

3. Methodology

3.1. Bias correction

The discrepancy in SWE between remote sensing and LSMs often arises due to uncertainties in the model physics and forcing data and satellite retrievals. These uncertainties can lead to a significant discrepancy in SWE between model simulations and satellite remote-sensing retrievals, potentially degrading performance. In previous studies (e.g., Reichle and Koster, 2004; Seo et al., 2021), a scaling method of the nonlinear cumulative distribution function (CDF) matching is used to account for the systematic bias of soil moisture in the model backgrounds. However, unlike soil moisture, SWE presents varying characteristics in the CDF distribution across different regions, such as between high and low latitudes, thus requiring the estimation of distribution at each grid point. As a result, the insufficient sample size hinders the clear simulation of the CDF distribution, posing challenges in its application. To address this issue, we attempted to apply a simple and effective standard normal deviation scaling to satellite-derived SWE at each grid point, considering its potential use as initial conditions for JULES LSM-based climate models. Based on the climatology and standard deviation for the model and remote sensing retrievals, the scaled SWE (O_{new}) from the satellite can be derived from the following relation:

$$O_{new} = \left(\frac{O-\bar{O}}{\sigma_o} \times \sigma_m\right) + \bar{M} \quad (1)$$

where $\bar{O}(\sigma_o)$ and $\bar{M}(\sigma_m)$ indicate climatology (standard deviation) of remote sensing retrievals and the model, respectively. This approach has been widely utilized in observation-based land initialization and has proven to be effective (e.g., Koster et al., 2011; Jeong et al., 2013).

3.2. Data assimilation method

The snow assimilation is conducted based on the LETKF (e.g., Hunt et al., 2007), which is utilized to combine remotely sensed retrievals with the LSM model outputs (a.k.a. backgrounds) at each grid point to produce a snow analysis. Unlike variational data assimilation methods, non-variational approaches (i.e., ensemble-based filters) characterize a probabilistic representation with the spread of the ensemble serving as an estimate of forecast uncertainty. LETKF has several advantages over other data assimilation methods. First, LETKF can efficiently handle large datasets and high-dimensional state variables by localizing the covariance matrix. This offers efficiency in parallel computing, making it suitable for real-time forecasting and high-resolution data assimilation. In this study, the horizontal local patch size and the localization length scale parameters are defined as 150 km and 30 km (Table 1), respectively. This approach involves the weight function for the covariance localization within the local patch centered at the analysis grid (e.g., Houtekamer and Mitchell, 2001; Hamill et al., 2001). This function assigns larger errors to observations located farther away from the center of the local patch, as proposed by Miyoshi and Yamane (2007), depending on the Gaussian function. Secondly, the method utilizes model simulation ensembles to capture the uncertainty in the initial states and background errors, which allows for a better representation of the flow-dependent probability distribution of the state variables that vary in time and space. Third, the LETKF employs an inflation parameter to adjust the ensemble spread, ensuring realistic uncertainty estimation by accounting for background errors. The underestimation of the analysis error covariance is typically issued by spatially and temporally constant boundary conditions and observation errors and limited ensemble members. Based on the standardized LETKF, this study applies a multiplicative covariance inflation of 20% of the spread of 24 member ensembles for each data assimilation cycle. Furthermore, the Kalman gain analysis (Seo et al., 2021), which quantifies the ratio of the background error to the total error

(equivalent to the sum of the background and the observation error), is conducted. This analysis serves to determine the weights assigned to assimilated observations in the analysis update processes of the LETKF.

3.3. Snow data assimilation design

This study conducts the advanced daily cycle snow data assimilation experiment at each ~~gird~~grid point using the LETKF based on the satellite data and the JULES LSM model outputs driven by 3-hourly JRA55 reanalysis atmospheric forcing. The snow assimilation processes are illustrated in Fig. 1, with a more detailed description in Table 1. Since data assimilation is conducted by considering the error of SWE in both the model and the observation, it is important to accurately understand the observation and background errors to improve the performance of data assimilation. The experiment calculates the background error from the 24 ensemble member spreads generated by perturbing atmospheric forcings such as longwave radiation, shortwave radiation, and precipitation in JULES LSM, as provided in section 2.3. Due to the absence of precise error estimates for AMSR2 SWE retrievals, the observation error is conservatively prescribed as 10% of AMSR2 SWE for each grid compared to the previous study utilizing AMSR2 SWE data (Lee et al., 2015), considering the general increase in the errors during the snow accumulation period with the development of deep snowpack (Foster et al., 2005; Cho et al., 2017). Here, the bias-corrected AMSR2 satellite data as described in section 3.1 is used as the observation data, and the updated snow analysis state through data assimilation becomes a new initial state for the next integration in JULES LSM (Fig. 1). In addition, the analysis state of this method is calculated based on the IMS snow cover fraction as follows (Fig. 1). If the SCF from IMS is 0, the snow analysis is set to zero; otherwise, it is derived through data assimilation. The reason for this is due to the importance of the presence or absence of snow in the climate system, as well as the high reliability of the IMS data (e.g.,

Brown et al., 2014). A background experiment of JULES LSM without satellite data assimilation as a baseline (referred to hereafter as "Openloop") is also achieved by employing the same ensemble perturbations, thereby measuring the skill improvement from the snow analysis state through the assimilation of satellite-derived SWE and IMS SCF from satellite and surface observations (referred to hereafter as "DA"). All experiments are conducted in April from 2013 to 2020, which is one of the months with low snow performance in the LSM when the snow begins to melt in the Northern Hemisphere (e.g., Toure et al., 2018; You et al., 2020).

4. Results

4.1. Skill Verification

Figure 2 displays the climatological-mean SCF from the IMS multi-satellite data (Brown et al., 2014) and the differences from IMS for AMSR2, Openloop, JRA55, and DA for April 2013-2020. Here, the JRA55 ~~SWE~~SCF serves as a reference dataset for comparison with other reanalyses and is associated with meteorological forcing data used in the JULES land surface model. April is a season when the accumulated snow during the cold season begins to melt. This study defines the transitional region with a climatological-mean SWE of less than 16 mm as in previous studies (e.g., Gan et al., 2021), the boundary of these transition regions is represented by the black lines in Fig. 2. The transitional regions exhibit large variability in space and time, and they are mainly located at mid-latitudes. The SCF climatology patterns show negligible differences in high latitudes of heavy snow accumulation but noticeable differences in the transitional mid-latitude regions of less snow. SCF from JRA55 tends to be underestimated compared to IMS, whereas AMSR2 and Openloop tend to overestimate. There is a clear difference in SCF between AMSR2 and IMS satellite data. This study gives more credibility to IMS than AMSR2, as the former is based on multiple satellite data sources (e.g., Brown et al., 2014). As we used the IMS SCF to define the snow region to be assimilated by AMSR2 SWE, it is natural that DA shows better consistency with IMS and reduces overestimation biases in Openloop. Quantitatively, the root mean square differences (accuracy, defined in supplementary Table 1 as in previous study) for AMSR2, Openloop, JRA55, and DA with (from) IMS are 0.23 (0.91), 0.18 (0.91), 0.13 (0.93), and 0.13 (0.97), respectively, showing the best consistency in DA. The quantitative differences between DA and other experimental results are minor, but noticeable spatial discrepancies exist, particularly around transition regions.

The SWE climatology from AMSR2, Openloop, JRA55, and DA is also compared with

CMC as a reference in Fig. 3. The SWE derived from AMSR2 shows a significant underestimation compared to CMC, particularly in the regions with heavy snow accumulation at high latitudes. This is presumed to be due to limitations in satellite sensors detecting the depth of snow (Gan et al., 2021). The SWE from JRA55 exhibits characteristics of overestimation in high latitudes and underestimation in transitional regions. On the other hand, the climatological SWEs from Openloop and DA exhibit higher correspondence to CMC, even higher than JRA55. Specifically, DA demonstrates a higher agreement with CMC, despite the marginal difference compared to Openloop. Quantitatively, the pattern correlation coefficients (root mean square differences) for AMSR2, Openloop, JRA55, and DA with (from) CMC are 0.63 (80.7 kg/m^2), 0.80 (50.1 kg/m^2), 0.60 (100.8 kg/m^2), and 0.80 (49.9 kg/m^2), respectively. Due to the application of standard deviation scaling to the satellite-derived SWE used in data assimilation, the discrepancy in climatological SWE distributions between DA and Openloop is deemed negligible. Despite its similarity to Openloop, DA with snow data assimilation displays the relatively highest correlation and the smallest root mean square difference among the datasets.

Next, we compare the temporal variation of SWE as measured by the Spearman rank correlation coefficient with CMC, which is regarded as more appropriate than the Pearson correlation coefficient for describing datasets containing nonlinearity and outliers such as snow in both time and space. Figure 4 compares the distribution of correlation skills from AMSR2, Openloop, JRA55, and DA. Openloop has a high performance in regions with heavy snow accumulation but relatively low performance in transition regions with significant snow changes. In contrast, the results from the AMSR2 satellite data represent poor performance in high-latitude areas with heavy snow accumulation but high performance in transitional regions, consistent with the previous studies (Gan et al., 2021). DA shows high performance not only in high-latitude areas with heavy snow accumulation but also in transition regions. Even

compared to JRA55 used as the atmospheric forcing, DA performs better in temporal variation. The quantitative results in the correlation in the Northern Hemisphere over 40°N (the transition region) are 0.41 (0.54) for AMSR2, 0.61 (0.48) for Openloop, 0.58 (0.58) for JRA55, and 0.67 (0.61) for DA, respectively. The findings indicate that satellite retrievals offer additional value in capturing temporal variations through data assimilation, indicating the benefit of assimilating the AMSR2 SWE despite the overall lower performance of the satellite data itself.

The performance improvement by DA is also evident in the zonally-averaged correlation coefficient shown in Fig. 5. The AMSR2 satellite data shows higher performance than Openloop in the transition region around latitude 45 °N-55 °N, although performance sharply decreases with increasing snow accumulation. Openloop indicates gradually increasing performance as the latitude increases, with the highest performance at around 60°N. DA denotes superior performance across the Northern Hemisphere, especially in the mid-latitude transition region than AMSR2 or JRA55. An exception is for 35-40°N in the Tibetan Plateau, where JRA55 used in-situ observations. The results suggest that the developed snow data assimilation system represents well not only the transitional regions but also the regions with high snow accumulation that are difficult to detect by satellite.

Figure 6 presents the Spearman rank correlation depending on the SWE amount in the Northern Hemisphere. AMSR2 exhibits higher performance than Openloop for SWE up to 16 mm. However, the performance of AMSR2 sharply declines beyond that threshold, and Openloop shows a better performance. Consistent with the results illustrated in Figs. 4 and 5, DA demonstrates superior performance compared to others. Note that DA performs significantly better in the transition region of less than 16 mm of SWE. Considering that the area below 16 mm of SWE accounts for approximately 53% of the entire area of the Northern Hemisphere(as shown in the pie chart in Fig. 6), the data assimilation impact is identifiable, and it can contribute substantially to the increase in the prediction skill through improving the

simulation of the albedo changes and surface energy balance.

Consistent with the description in Section 3.3, this study considers an algorithm based on the highly reliable IMS satellite SCF data to identify the presence of snow and determine the assimilation process. Therefore, a further sensitivity test is conducted to investigate the influence of incorporating IMS data in snow assimilation. Figure 7 compares the correlation differences between Openloop and the data assimilation result employing both AMSR2 and IMS (DA), as well as the data assimilation result utilizing solely AMSR2 and excluding IMS (hereafter referred to as DA_AMSR2). The results obtained from the snow assimilation show the improvements in the transitional regions where AMSR2 denotes a better agreement with the observations compared to Openloop. Notably, the skill is enhanced significantly in DA by incorporating the IMS SCF. DA exhibits inferior performance compared to Openloop in certain exceptional cases, which may be attributed to discrepancies in snow identification between the CMC observations used for correlation and the IMS data utilized for data assimilation. Moreover, the performance of SWE improves even when only AMSR2 is used, but incorporating IMS leads to a substantial improvement in the transitional regions. This implies that IMS has a positive influence on the snow data assimilation.

4.2 Kalman gain analysis

In order to better understand the skill enhancement through snow assimilation of satellite data, this section examines the Kalman gain. Figure 8 illustrates the spatial distribution of observation error, model background error, and the Kalman gain for SWE. A high value of the Kalman gain denotes that the assimilated result is closer to the AMSR2 observation than the model background. The Kalman gain is large when the background error becomes large, or the observation error is small. As this study specifies the observation error as a conservative 10% of SWE compared to the previous study (Lee et al., 2015), the observation error basically

follows the distribution similar to the climatological-mean values. The background errors, originating from the 24 ensemble members, have higher values in high-latitude regions and mid-latitude regions. Data assimilation methods such as LETKF used in this study often face challenges in accurately representing background errors when the ensemble spread is insufficient. Generally, the magnitude of ensemble spread is frequently compared to the root mean square error (RMSE). The ensemble spread in this study demonstrates a sufficiently valid magnitude in comparison with the RMSE, as illustrated in SFig. 1, indicating that it is well estimated. Moreover, the standardized distribution of SWE among the ensemble members exhibits a quasi-Gaussian distribution centered around zero, with the transition region showing a closer resemblance to a standardized Gaussian distribution (SFig. 4). In the spatial distribution of Kalman gain in Fig. 8c, significant performance improvement is observed in transition regions, where Kalman gains exhibit larger values. However, in high-latitude areas with substantial snow accumulation, there is a tendency for Kalman gain to have lower values. These findings agree well with the bar graph in Fig. 9, which illustrates the Kalman gain as a function of SWE amount. In the region encompassing the transition region with SWE amounts below 20 mm, the Kalman gain displays the highest values, particularly exceeding 0.8. As the SWE amount increases, the Kalman gain decreases, with a significant decline observed when the SWE amount reaches 80-100 mm or higher. Furthermore, in the areas where DA denotes improved skill compared to Openloop, the Kalman gain shows values generally above 0.7. In contrast, relatively lower values below 0.5 are observed in the areas with decreased skill. This indicates that in the dominant areas of performance improvement, including the transition region, the background error is significantly larger than the observation error, emphasizing the substantial influence of observations in data assimilation. It is found that accurate remote sensing retrievals are well reflected in regions with high uncertainty in the LSM through the snow data assimilation system, leading to performance improvement.

4.3 Validation of the SWE for the extreme event

In April 2020, Siberia experienced a record-breaking heatwave with the highest observed average temperature. This section investigates the potential benefits of snow assimilation using satellite data for the case of the 2020 Siberian heatwave. Previous studies have identified the strong polar vortex accompanied by the AO amplification during winter as a major cause of the cold Eurasian region (Overland and Wang, 2021). Additionally, it has been revealed that the occurrence of high temperatures in the Siberian region is found to be closely associated with large-scale atmospheric waves in the upper atmosphere over the Eurasian region originating from the Atlantic (De Angelis et al., 2023). As a result, remarkable snow melting occurred due to the high surface temperature over the Siberian region in April 2020, leading to extremely low values of SWE and SCF as depicted in SFig. 2. This is consistent with previous studies reporting a significant snow depletion in 2020 in the region (Gloege et al., 2022). Especially, as shown in Fig. 10, significant negative anomalies in SWE and SCF are predominant over the transition region. Substantial snow melt can contribute to record-breaking heatwaves through albedo feedback and changes in the ratio of the latent and sensible heat fluxes from the exposed surface, coupled with favorable atmospheric circulation patterns (Collow et al., 2022). Collow et al. (2022) demonstrated that the exposed surface contributed to up to 20% of the temperature anomaly over Siberia in spring 2020. This implies the importance of realistic snow initial states in the global coupled model forecasts. For the Siberian region with extreme high-temperature events marked by the red box in Fig. 10, DA shows a better agreement with the extremely dry snow conditions, especially in the transitional region, compared to the Openloop. These results are evident when considering the observation-to-model ratio in that region. The percentage of CMC (IMS) is 83% (78%) for Openloop and 93% (89%) for DA, indicating that DA with snow data assimilation based on satellite data effectively replicates the observed snow depletion in comparison with Openloop. Similarly to

the 2020 case, we obtained another significant case in 2014 compared to Openloop, as shown in SFig. 3. Such extremely dry snow conditions can provide significant heatwave events in the following months.

5. Conclusions and discussion

The advanced SWE data assimilation is developed in this study with the LETKF data assimilation method and the JULES LSM. The system assimilates snow water equivalent retrievals from AMSR2 and IMS snow cover. This constitutes an objective way to optimally combine two imperfect data sources for SWE from satellite remote sensing data and the land surface model simulation forced by observed atmospheric data. This study shows that the satellite-derived SWE has limitations in penetrating deep snow and exhibited much discrepancy from the SWE obtained from the Openloop LSM simulations. The SWE assimilation in this study proves the beneficial impacts of using satellite snow data, maintaining better analysis quality by dynamically balancing the errors from the satellite observations and the model background states.

It is found that the simulation from Openloop as a baseline shows superior performance in high-latitude regions with heavy snow accumulation but relatively inferior performance in transition regions with much variation of snow in space and time. Contrastingly, the AMSR2 satellite data represent poor performance in high-latitude regions but exhibit relatively better performance in the transition regions. The SWE from the LETKF data assimilation consistently exhibits better performance in capturing the climatology and temporal variation compared to other results. It specifically improves the analysis in the mid-latitude transition regions that cover approximately 53% of the entire areas of the Northern Hemisphere. It is found that the model background errors estimated from the ensemble spread are significantly larger than the observation errors, thereby reflecting satellite information more in those regions. The LETKF data assimilation also proves reliable representation in the heavy snow regions due to low ensemble spread and large uncertainty in the satellite retrievals. Moreover, during the record-breaking heatwave in Siberia in April 2020, the remarkable snow depletion observed due to high surface temperatures is more realistically reproduced by our snow analysis compared to

the Openloop.

This snow data assimilation framework is anticipated to contribute to a more precise prediction of atmospheric conditions by realistically capturing the interaction between the atmosphere and land, given the substantial influence of SWE on energy and water balance at the interface of the atmosphere and land. Specifically, this applies to the transitional regions with high spatial and temporal variability. The long-term analysis of snow manifests a pronounced variability in the continental interior at the interannual timescales, potentially improving the prediction of extreme heatwave events by global climate models. This study used the gridded CMC data from in-situ observations for the validation. Although existing snow data are subject to much uncertainty and limitations, we expect to obtain comparable conclusions and significant benefits of optimally combining satellite SWE data and the LSM model simulations through LETKF data assimilation method.

The quality of the observation is crucial in the data assimilation system. Satellite-derived snow cover exhibits a significantly higher accuracy compared to other data sources, while SWE has restricted performance due to the limitations of penetration depth by satellite sensors and relies heavily on estimation algorithms. Due to these problems, most previous studies and operational centers primarily depend on satellite-derived snow cover for snow initialization. However, the findings from this study highlighted the beneficial impacts of using satellite-derived SWE, particularly in the rapidly changing transition areas, to find out which variable is more important in closing surface energy and water balance changed by snow. Nevertheless, areas of significance in large-scale circulation, such as the Tibetan region, which experiences significant uncertainty and degraded performance in satellite data, do not exhibit substantial data assimilation effects. As the performance of SWE derived from various satellites continues to advance, these issues will be discussed more.

Key words

Snow data assimilation, AMSR2, LETKF, snow water equivalent, JULES LSM

Data availability.

The AMSR2 SWE and IMS SC were obtained from https://n5eil01u.ecs.nsidc.org/AMSA/AU_DySno.001/ and https://noaadata.apps.nsidc.org/NOAA/G02156/, respectively. The CMC SWE was collected from https://daacdata.apps.nsidc.org/pub/DATASETS/nsidc0447_CMC_snow_depth_v01/. The snow-assimilated results and land surface variables from the LSM offline simulation may be requested from the authors.

Author contributions.

LJL conceived the project, designed the study, developed the snow assimilation system, wrote the paper, and made the figures. LMI provided advice on the methods, project design, and review and editing of the manuscript. TSL helped with the experiment with the land surface model. SEK helped with the data assimilation method based on LETKF. LYK provided advice on snow satellite data and the sensitivity methods. All authors contributed to the writing of the paper by providing comments and feedback.

Competing interests.

The contact author has declared that none of the authors has any competing interests.

Acknowledgements

This work was funded by the Korea Meteorological Administration Research and Development Program under Grant ~~KMI2021-01210.~~(RS-2024-00403698). ES was supported by Learning & Academic research institution for Master's·PhD students, and Postdocs (LAMP) Program of the National Research Foundation of Korea (NRF) grant funded by the Ministry of Education (RS-2023-000301702). We thank the supercomputing resources of the UNIST Supercomputing Center.

Reference

Allen, R.J., Zender, C.S.: Forcing of the Arctic Oscillation by Eurasian snow cover. J. Clim. 24 (24), 6528-6539, 2011.

Best, M.J., Pryor, M., Clark, D.B., Rooney, G.G., Essery, R., Ménard, C.B., Edwards, J.M., Hendry, M.A., Porson, A., Gedney, N., Mercado, L.M., Sitch, S., Blyth, E., Boucher, O., Cox, P.M., Grimmond, C.S.B., Harding, R.J.: The Joint UK Land Environment Simulator (JULES), model description–Part 1: energy and water fluxes. Geosci. Model Dev. 4, 677–699, 2011.

Boone, A., Habets, F., Noilhan, J., Clark, D., Dirmeyer, P., Fox, S., Gusev, Y., Haddeland, I., Koster, R., Lohmann, D., Mahanama, S., Mitchell, K., Nasonova, O., Niu, G.Y., Pitman, A., Polcher, J., Shmakin, A., Tanaka, K., van den Hurk, B., Ve´ rant, S., Verseghy, D., Viterbo, P., Yang, Z.L.: The Rhone-Aggregation land surface scheme intercomparison project: an overview. J. Clim. 17, 187–208, 2004.

Brasnett, B.: A global analysis of snow depth for numerical weather prediction. J. Appl. Meteorol. 38 (6), 726–740, 1999.

Brown, L.C., Howell, S.E., Mortin, J., Derksen, C.: Evaluation of the Interactive Multisensor Snow and Ice Mapping System (IMS) for monitoring sea ice phenology. Remote Sens. Environ. 147, 65–78. doi: 10.1016/j.rse.2014.02.012, 2014.

Brown, R.D., Brasnett, B.: Canadian Meteorological Centre (CMC) Daily Snow Depth Analysis Data. NASA National Snow and Ice Data Center Distributed Active Archive Center, Boulder, Colorado, USA. https://doi.org/10.5067/ W9FOYWH0EQZ3, 2010.

Brown, R.D., Brasnett, B., Robinson, D.: Gridded North American monthly snow depth and snow water equivalent for GCM evaluation. Atmos.–Ocean, 41, 1–14, 2003.

Broxton, P.D., Zeng, X., Dawson, N.: The impact of a low bias in snow water equivalent initialization on CFS seasonal forecasts. J. Clim. 30 (21), 8657–8671. https://doi.org/10.1175/JCLI-D-17-0072.1, 2017.

Brubaker, K., Pinker, R., Deviatova, E.: Evaluation and comparison of MODIS and IMS snow-cover estimates for the continental United States using station data. J. Hydrometeorol. 6, 1002–1017, 2009.

Burke, E. J., Dankers, R., Jones, C. D., and Wiltshire, A. J.: A retrospective analysis of pan Arctic permafrost using the JULES land surface model, Clim. Dynam., 41, 1025–1038, https://doi.org/10.1007/s00382-012-1648-x, 2013.

Chen, M., Wang, W., Kumar, A.: Prediction of monthly-mean temperature: The roles of atmospheric and land initial conditions and sea surface temperature J. Clim. 23(3), 717-725, 2010.

Cho, E., Tuttle, S.E., Jacobs, J.M.: Evaluating consistency of snow water equivalent retrievals from passive microwave sensors over the north central US: SSM/I vs. SSMIS and AMSR-E vs. AMSR2. Remote Sens. 9(5), 465, 2017.

Cohen, J., Barlow, M., Kushner, P. J., Saito, K.: Stratosphere–troposphere coupling and links with eurasian land surface variability. J. Clim. 20(21), 5335–5343. https://doi.org/10.1175/2007jcli1725.1, 2007.

Collow, A.B.M., Thomas, N.P., Bosilovich, M.G., Lim, Y.K., Schubert, S.D., Koster, R.D.: Seasonal variability in the mechanisms behind the 2020 Siberian heatwaves. J. Clim. 35(10), 3075-3090, 2022.

Dawson, N., Broxton, P., Zeng, X.: Evaluation of remotely sensed snow water equivalent and snow cover extent over the contiguous United States. J. Hydrometeorol. 19 (11), 1777–1791. https://doi.org/10.1175/JHM-D-18-0007.1, 2018.

De Angelis, A.M., Schubert, S.D., Chang, Y., Lim, Y.K., Koster, R.D., Wang, H., Marquardt Collow, A.B.: Dynamical Drivers of the Exceptional Warmth over Siberia during the Spring of 2020. J. Clim. 36(15), 4837-4861, 2023.

De Lannoy, G.J.M., Reichle, R.H., Houser, P.R., Arsenault, K.R., Verhoest, N.E.C., Pauwels, V.R.N.: Satellite-scale snow water equivalent assimilation into a high-resolution land surface model. J. Hydrometeorol. 11 (2), 352–369. https://doi. org/10.1175/2009JHM1192.1, 2010.

De Rosnay, P., Balsamo, G., Albergel, C., Muñoz-Sabater, J., Isaksen, L. Initialisation of land surface variables for numerical weather prediction. Surv. Geophys. 35, 607-621, 2014.

Dee, D., Uppala, S., Simmons, A., Berrisford, P., Poli, P., Kobayashi, S., Andrae, U., Balsameda, M., Balsamo, G., Bauer, P., Bechtold, P., Beljaars, A.C.M., van de Berg, L., Bidlot, J., Bormann, N., Delsol, C., Dragani, R., Fuentes, M., Geer, A.J., Haimberger, L., Healy, S.B., Hersbach, H., Hólm, E.V., Isaksen, L., Kållberg, P., Köhler, M., Matricardi, M., McNally, A.P., Monge-Sanz, B.M., Morcrette, J.-J., Park, B.-K., Peubey, C., de Rosnay, P., Tavolato, C., Thépaut, J.-N., Vitart, F.: The ERA-Interim reanalysis: Configuration and performance of the data assimilation system. Q. J. R. Meteorol. Soc. 137, 553–597, 2011.

Derome J, Lin H, Brunet, G.: Seasonal forecasting with a simple general circulation model: Predictive skill in the AO and PNA. J. Clim., 15, 597–609, 2005.

Dirmeyer, P.A.: The terrestrial segment of soil moisture–climate coupling. Geophys. Res. Lett. 38(16), 2011.

Dirmeyer, P.A., Gao, X., Zhao, M., Guo, Z., Oki, T., Hanasaki, N.: The Second Global Soil Wetness Project (GSWP-2): Multi-model analysis and implications for our perception of the land surface. Bull. Amer. Meteor. Soc. 87, 1381–1397, 2006.

Dutra, E., Schär, C., Viterbo, P., Miranda, P. M.: Land-atmosphere coupling associated with snow cover. Geophys. Res. Lett. 38 (15) , 2011.

Dziubanski, D.J., Franz, K.J.: Assimilation of AMSR-E snow water equivalent data in a spatially-lumped snow model. J. Hydrol. 540, 26–39. https://doi.org/10.1016/j.jhydrol.2016.05.046, 2016.

Essery, R.L.H., Rutter, N., Pomeroy, J., Baxter, R., Stahli, M., Gustafsson, D., Barr, A., Bartlett, P., Elder, K.: SNOWMIP2: an evaluation of forest snow process simulations. Bull. Amer. Meteor. Soc. 90, 1120–1135, 2009.

Eagleson, P.S.: Dynamic Hydrology, McGraw-Hill, 1970

Foster, J.L., Sun, C., Walker, J.P., Kelly, R., Chang, A., Dong, J., Powell, H.: Quantifying the uncertainty in passive microwave snow water equivalent observations. Remote Sens. Environ. 94, 187–203, 2005.

Gan, Y., Zhang, Y., Kongoli, C., Grassotti, C., Liu, Y., Lee, Y. K., Seo, D. J.: Evaluation and blending of

673 ATMS and AMSR2 snow water equivalent retrievals over the conterminous United
674 States. Remote Sens. Environ. 254, 112280, 2021.
675 Girotto, M., Musselman, K. N., and Essery, R. L. H.: Data Assimilation Improves Estimates of Climate-
676 Sensitive Seasonal Snow, Current Climate Change Reports, 6, 81–94,
677 https://doi.org/10.1007/s40641-020-00159-7, 2020.
678 Gloege, L., Kornhuber, K., Skulovich, O., Pal, I., Zhou, S., Ciais, P., Gentine, P.: Land-Atmosphere Cascade
679 Fueled the 2020 Siberian Heatwave. AGU Advances, 3 (6), e2021AV000619, 2022.
680 Hamill, T.M., Whitaker, J.S., Snyder, C.: Distance-dependent filtering of background error covariance
681 estimates in an ensemble Kalman filter. Mon. Weather Rev. 129, 2776–2790, 2001.
682 Helfrich, S.R., McNamara, D., Ramsay, B.H., Baldwin, T., Kasheta, T.: Enhancements to, and forthcoming
683 developments in the interactive multisensor snow and ice mapping system (IMS). Hydrol.
684 Process. 21 (12), 1576–1586. https:// doi.org/10.1002/hyp.6720, 2007.
685 Helmert, J., Şensoy Şorman, A., Montero, R.A., De Michele, C., De Rosnay, P., Dumont, M., Finger, D.,
686 Lange, M., Picard, G., Potopová, V., et al.: Review of Snow Data Assimilation Methods for
687 Hydrological, Land Surface, Meteorological and Climate Models: Results from a COST
688 HarmoSnow Survey. Geoscience, 8 (12), 489, 2018.
689 Houtekamer, P.L., Mitchell, H.L.: A sequential ensemble Kalman filter for atmospheric data
690 assimilation. Mon. Weather Rev. 129, 123–137, 2001.
691 Huning, L.S., AghaKouchak, A.: Global snow drought hot spots and characteristics. Proc. Natl. Acad.
692 Sci. 117(33), 19753-19759, 2020.
693 Hunt, B.R., Kostelich, E.J., Szunyogh, I.: Efficient data assimilation for spatiotemporal chaos: a local
694 ensemble transform Kalman filter. Phys. D Nonlinear Phenom. 230, 112–126, 2007.
695 Imaoka, K., Kachi, M., Kasahara, M., Ito, N., Nakagawa, K., Oki, T.: Instrument performance and
696 calibration of AMSR-E and AMSR2. Int. Arch. Photogramm. Remote. Sens. Spat. Inf. Sci. 38
697 (8), 13–16, 2010.
698 Jeong, J.H., Linderholm, H.W., Woo, S.H., Folland, C., Kim, B.M., Kim, S.J., Chen, D.: Impacts of snow
699 initialization on subseasonal forecasts of surface air temperature for the cold season. J.
700 Clim. 26 (6), 1956-1972, 2013.
701 Kobayashi, S., Ota, Y., Harada, Y., Ebita, A., Moriya, M., Onoda, H., Onogi, K., Kamahori, H., Kobayashi,
702 C., Endo, H.: The JRA-55 reanalysis: general specifications and basic characteristics. J.
703 Meteorol. Soc. Jpn. Ser. II 93, 5–48, 2015.
704 Koster, R.D., Dirmeyer, P.A., Guo, Z., Bonan, G., Chan, E., Cox, P., Gordon, C.T., Kanae, S., Kowalczyk,
705 E., Lawrence, D., Liu, P., Lu, C.H., Malyshev, S., McAvaney, B., Mitchell, K., Mocko, D., Oki,
706 T., Oleson, K., Pitman, A., Sud, Y.C., Taylor, C.M., Verseghy, D., Vasic, R., Xue, Y., Yamada,
707 T., GLACE Team: Regions of strong coupling between soil moisture and
708 precipitation. Science, 305 (5687), 1138–
709 1140, https://doi.org/10.1126/science.1100217, 2004.
710 Koster, R.D., Mahanama, S., Yamada, T., Balsamo, G., Berg, A., Boisserie, M., Dirmeyer, P., Doblas-Reyes,
711 F., Drewitt, G., Gordon, C.: The second phase of the global land–atmosphere coupling

712 experiment: soil moisture contributions to subseasonal forecast skill. J. Hydrometeorol. 12,
713 805–822, 2011.
714 Kumar, S.V., Jasinski, M., Mocko, D.M., Rodell, M., Borak, J., Li, B., Beaudoing, H.K., Peters-Lidard, C.D.:
715 NCA-LDAS land analysis: development and performance of a multisensor, multivariate land
716 data assimilation system for the national climate assessment. J. Hydrometeorol. 20 (8), 1571–
717 1593. https://doi.org/10.1175/JHM-D- 17-0125.1, 2019.
718 Kwon, Y., Yang, Z.-L., Hoar, T.J., Toure, A.M.: Improving the radiance assimilation performance in
719 estimating snow water storage across snow and land-cover types in North America. J.
720 Hydrometeorol. 18 (3), 651–668. https://doi.org/10.1175/JHM-D-16-0102.1, 2017.
721 Lee, Y.K., Kongoli, C., Key, J.: An in-depth evaluation of heritage algorithms for snow cover and snow
722 depth using AMSR-E and AMSR2 measurements. J. Atmos. Ocean. Technol. 32(12), 2319-
723 2336, 2015.
724 Li, F., Orsolini, Y.J., Keenlyside, N., Shen, M.L., Counillon, F., Wang, Y.G.: Impact of snow initialization
725 in subseasonal-to-seasonal winter forecasts with the Norwegian Climate Prediction
726 Model. J. Geophys. Res. Atmos. 124 (17-18), 10033-10048, 2019.
727 Li, F., Wang, H.: Autumn Eurasian snow depth, autumn Arctic sea ice cover and East Asian winter
728 monsoon. Int. J. Climatol. 34(13), 3616-3625, 2014.
729 Lim, S., Gim, H.J., Lee, E., Lee, S., Lee, W.Y., Lee, Y.H., Cassardo C., Park, S.K.: Optimization of snow-
730 related parameters in the Noah land surface model (v3. 4.1) using a micro-genetic algorithm
731 (v1. 7a). Geosci. Model Dev. 15(22), 8541-8559, 2022.
732 Liu, Y., Peters-Lidard, C.D., Kumar, S.V., Arsenault, K.R., Mocko, D.M.: Blending satellite-based snow
733 depth products with in situ observations for streamflow predictions in the upper Colorado
734 River basin. Water Resour. Res. 51 (2), 1182–1202. https://doi.org/10.1002/2014WR016606,
735 2015.
736 Luojus, K., Pulliainen, J., Takala, M., Lemmetyinen, J., Mortimer, C., Derksen, C., Mudryk, L., Moisander,
737 M., Hiltunen, M., Smolander, T., Ikonen, J., Cohen, J., Salminen, M., Norberg, J., Veijola, K., and
738 Venäläinen, P.: GlobSnow v3.0 Northern Hemisphere snow water equivalent dataset, Sci. Data,
739 8, 163, https://doi.org/10.1038/s41597-021-00939-2, 2021.
740 Meng, J., Yang, R., Wei, H., Ek, M., Gayno, G., Xie, P., Mitchell, K.: The land surface analysis in the
741 NCEP climate forecast system reanalysis. J. Hydrometeorol. doi:10.1175/JHM-D-11-090.1,
742 2012.
743 Meyal, A.Y., Versteeg, R., Alper, E., Johnson, D., Rodzianko, A., Franklin, M., Wainwright, H.: Automated
744 cloud based long short-term memory neural network based SWE prediction. Front. Water, 2,
745 574917, 2020.
746 Miyoshi, T., Yamane, S.: Local ensemble transform Kalman filtering with an AGCM at a T159/L48
747 resolution. Mon. Weather Rev. 135, 3841–3861, 2007.
748 Oaida, C. M., Reager, J. T., Andreadis, K. M., David, C. H., Levoe, S. R., Painter, T. H., Bormann, K. J.,
749 Trangsrud, A. R., Girotto, M., and Famiglietti, J. S.: A High-Resolution Data Assimilation
750 Framework for Snow Water Equivalent Estimation across the Western United States and

751 Validation with the Airborne Snow Observatory, J. Hydrometeorol., 20, 357–378,
752 https://doi.org/10.1175/JHM-D-18-0009.1, 2019.
753 Orsolini, Y.J., Senan, R., Balsamo, G., Doblas-Reyes, F.J., Vitart, F., Weisheimer, A., Carrasco, A., Benestad,
754 R.E.: Impact of snow initialization on sub-seasonal forecasts. Clim. Dyn. 41, 1969-1982, 2013.
755 Orsolini, Y.J., Senan, R., Vitart, F., Weisheimer, A., Balsamo, G., Doblas-Reyes, F.: Influence of the
756 Eurasian snow on the negative North Atlantic Oscillation in subseasonal forecasts of the
757 cold winter 2009/10. Clim. Dyn. 47(3-4), 1325–1334. https://doi.org/10.1007/s00382-015-
758 2903-8, 2016.
759 Overland, J. E., Wang, M.: The 2020 Siberian heat wave. Int. J. Climatol. 41, E2341-E2346, 2021.
760 Pullen, S., Jones, C., Rooney, G.: Using satellite-derived snow cover data to implement a snow analysis
761 in the met office NWP model. J. Appl. Meteorol. 50, 958–973. doi:10.1175/2010JAMC2527.1,
762 2011.
763 Pulliainen, J., Luojus, K., Derksen, C., Mudryk, L., Lemmetyinen, J., Salminen, M., Ikonen, J., Takala, M.,
764 Cohen, J., Smolander, T., Norberg, J.: Patterns and trends of Northern Hemisphere snow mass
765 from 1980 to 2018. Nature, 581 (7808), 294–298. https://doi.org/10.1038/s41586-020-2258-
766 0, 2020.
767 Ramsay, B.H.: The interactive multisensor snow and ice mapping system. Hydrol. Process. 12 (10-11),
768 1537–1546, 1998.
769 Reichle, R.H.: Data assimilation methods in the Earth sciences. Adv. Water Resour. 31, 1411–1418,
770 2008.
771 Reichle, R.H., Draper, C.S., Liu, Q., Girotto, M., Mahanama, S.P., Koster, R.D., De Lannoy, G.J.:
772 Assessment of MERRA-2 land surface hydrology estimates. J. Clim. 30 (8), 2937-2960, 2017.
773 Reichle, R.H., Koster, R.D.: Bias reduction in short records of satellite soil moisture. Geophys. Res. Lett.
774 31, 2004.
775 Reichle, R.H., Koster, D., De Lannoy, G.J.M., Forman, B.A., Liu, Q., Mahanama, S.P.P., Toure, A.M.:
776 Assessment and Enhancement of MERRA Land Surface Hydrology Estimates. J. Clim. 24,
777 6322–6338, 2011.
778 Seo, E., Lee, M.I., Jeong, J.H., Koster, R.D., Schubert, S.D., Kim, H.M., Kim, D.H., Kang H.S., Kim, H.K.,
779 MacLachlan, C., Scaife, A.A.: Impact of soil moisture initialization on boreal summer
780 subseasonal forecasts: mid-latitude surface air temperature and heat wave
781 events. Clim. Dyn. 52, 1695-1709, 2019.
782 Seo, E., Lee, M.I., Reichle, R.H.: Assimilation of SMAP and ASCAT soil moisture retrievals into the
783 JULES land surface model using the Local Ensemble Transform Kalman Filter. Remote Sens.
784 Environ. 253, 112222, 2021.
785 Seo, E., Lee, M.I., Schubert, S.D., Koster, R.D., Kang, H.S.: Investigation of the 2016 Eurasia heat wave
786 as an event of the recent warming. Environ. Res. Lett. 15(11), 114018, 2020.
787 Shlyaeva, A., Tolstykh, M., Mizyak, V., Rogutov, V.: Local ensemble transform Kalman filter data
788 assimilation system for the global semi-Lagrangian atmospheric model. Russ. J. Numer. Anal.
789 Math. Model. 28(4), 419-442, 2013.

790 Smyth, E. J., Raleigh, M. S., and Small, E. E.: Improving SWE Estimation With Data Assimilation: The
791 Influence of Snow Depth Observation Timing and Uncertainty, Water Resour. Res., 56,
792 e2019WR026853, https://doi.org/10.1029/2019WR026853, 2020.
793 Sturm, M., Taras, B., Liston, G.E., Derksen, C., Jonas, T., Lea, J.: Estimating snow water equivalent using
794 snow depth data and climate classes. J. Hydrometeor. 11, 1380–1394, 2010.
795 Su, H., Yang, Z.-L., Dickinson, R.E., Wilson, C.R., Niu, G.-Y.: Multisensor snow data assimilation at the
796 continental scale: The value of gravity recovery and climate experiment terrestrial water
797 storage information. J. Geophys. Res., 115, D10104, doi:10.1029/2009JD013035, 2010.
798 Takala, M., Luojus, K., Pulliainen, J., Derksen, C., Lemmetyinen, J., Karna, J.P., Koskinen, J., Bojkov, B.:
799 Estimating northern hemisphere snow water equivalent for climate research through
800 assimilation of space-borne radiometer data and ground-based measurements. Remote
801 Sens. Environ. 115:3517–3529, 2011.
802 Thomas, J.A., Berg, A.A., Merryfield, W.J.: Influence of snow and soil moisture initialization on sub-
803 seasonal predictability and forecast skill in boreal spring. Clim. Dyn. 47 (1), 49-65, 2016.
804 Toure, A.M., Luojus, K., Rodell, M., Beaudoing, H., Getirana, A.: Evaluation of simulated snow and
805 snowmelt timing in the Community Land Model using satellite-based products and
806 streamflow observations. J. Adv. Model. Earth Syst. 10(11), 2933-2951, 2018.
807 U.S. National Ice Center: IMS daily Northern Hemisphere snow and ice analysis at 1 km, 4 km, and
808 24 km resolutions, version 3. Boulder, Colorado, USA. NSIDC: National Snow and Ice Data
809 Center, accessed: 18 Aug 2022, https://doi.org/10.7265/N52R3PMC, 2008.
810 You, Y., Huang, C., Gu, J., Li, H., Hao, X., Hou, J.: Assessing snow simulation performance of typical
811 combination schemes within Noah-MP in northern Xinjiang, China. J. Hydrol. 581, 124380,
812 2020.
813

814 **Table 1**. Description of the land surface model, the data used, and assimilation experiment
815 designs.

	INFORMATION	REFERENCES
Land Surface Model	JULES	Best et al., (2011)
Atmospheric Forcing	3-hourly JRA-55 reanalysis	Kobayashi et al., (2015)
Snow Observation	AMSR2 & IMS	Imaoka et al., (2010) Ramsay (1998) Helfrich et al., (2007)
Data Assimilation scheme	Local Ensemble Transform Kalman Filter (LETKF)	Hunt et al., (2007) Miyoshi and Yamane, (2007)
Resolution (km)	0.5° ×0.5° (~ 50)	
	1-day DA cycle	
Localization patch size (km)	3×3 (150), σ =30	
Ensemble sizes	24	
Experiment period	2013-2020, APR	

816

817

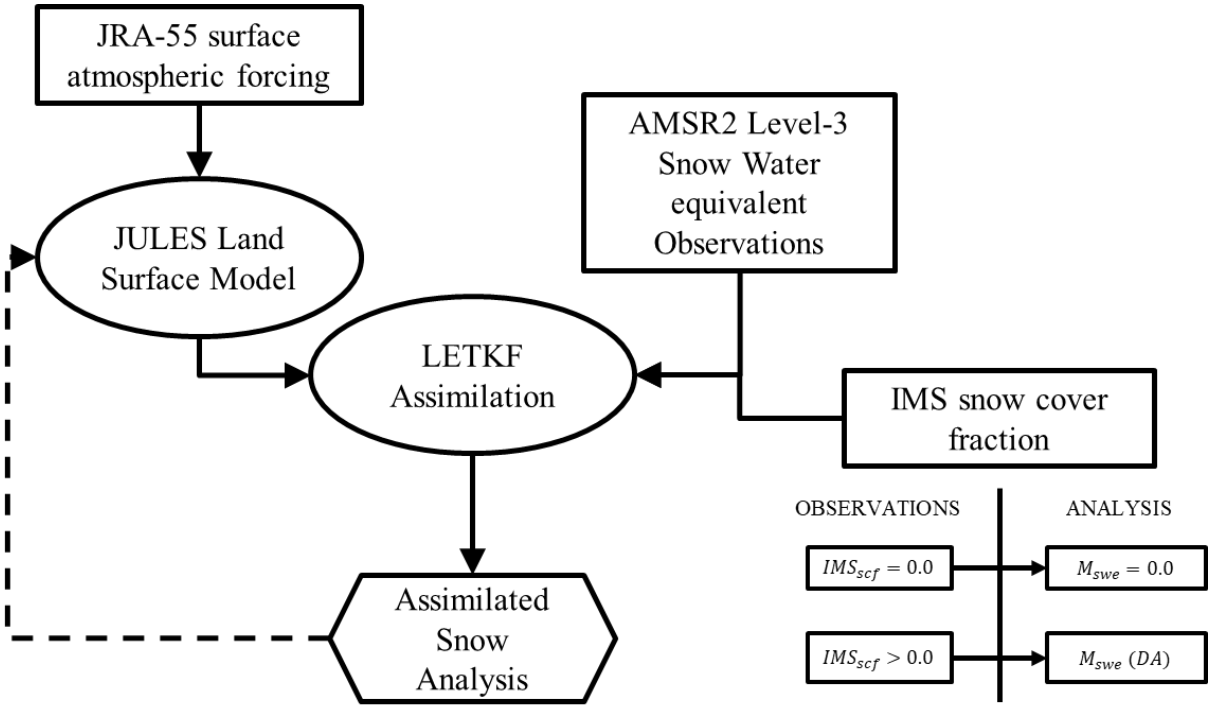

818

819 **Figure 1**. Schematic diagram of the snow assimilation system with satellite-derived

820 observations and the land surface model outputs.

821

822

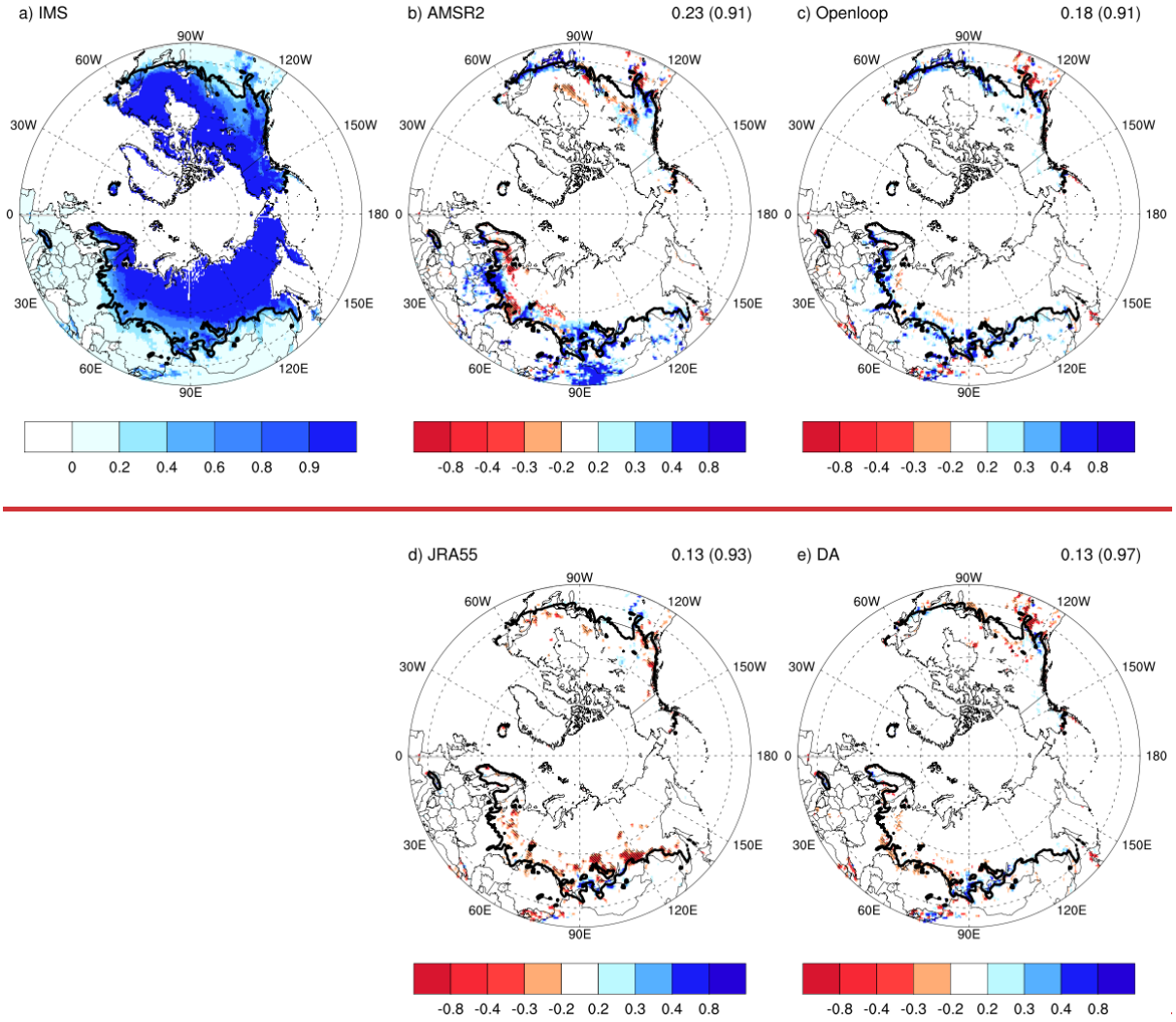
a) IMS
b) AMSR2
0.23 (0.91)
c) Openloop
0.18 (0.91)
d) JRA55
0.13 (0.93)
e) DA
0.13 (0.97)
90W
60W
120W
30W
150W
0
180
30E
150E
60E
120E
90E
0 0.2 0.4 0.6 0.8 0.9
-0.8 -0.4 -0.3 -0.2 0.2 0.3 0.4 0.8

823

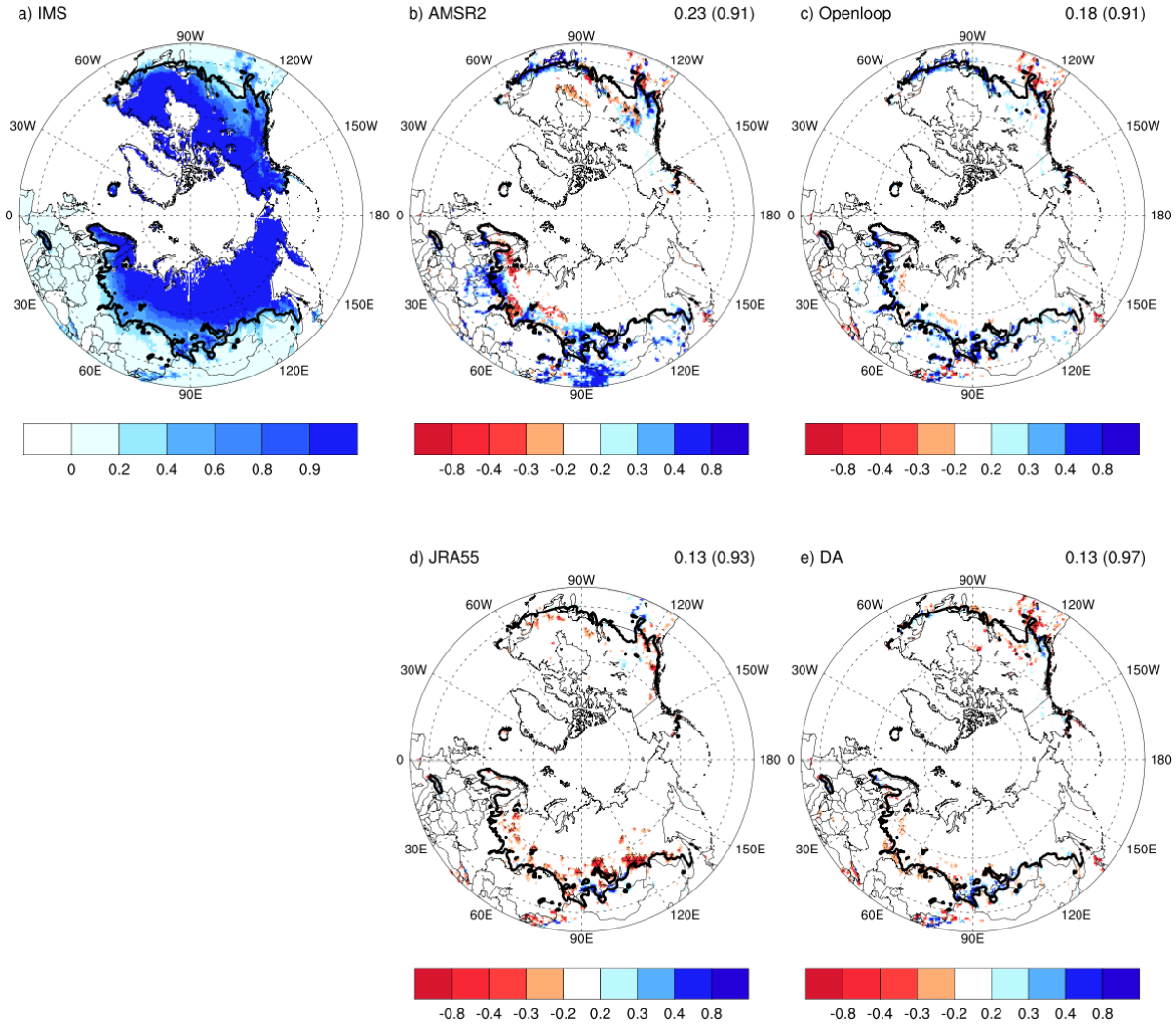

824

825 **Figure 2.** (a) Climatology of SCF from IMS used as reference and (b-e) the differences from
826 IMS for AMSR2, base-line model simulation (Openloop), JRA55, and the data
827 assimilation results (DA) for April during 2013-2020. The black line represents the
828 boundary of the transition region, defined as the climatological-mean SWE of less than
829 16mm. Each value on the top right is the root-mean-squared difference with IMS and
830 the accuracy from IMS (parenthesis) for 15323 pixels over 40-60°N. The accuracy is
831 defined in supplementary Table 1 as in previous study (Lee et al., 2015). Negative
832 values (areas) in red shades are indicated with ~~a diagonal line~~hatching. Here, SCF is
833 dimensionless since it represents a proportion rather than a physical measurement with
834 units.

835

836

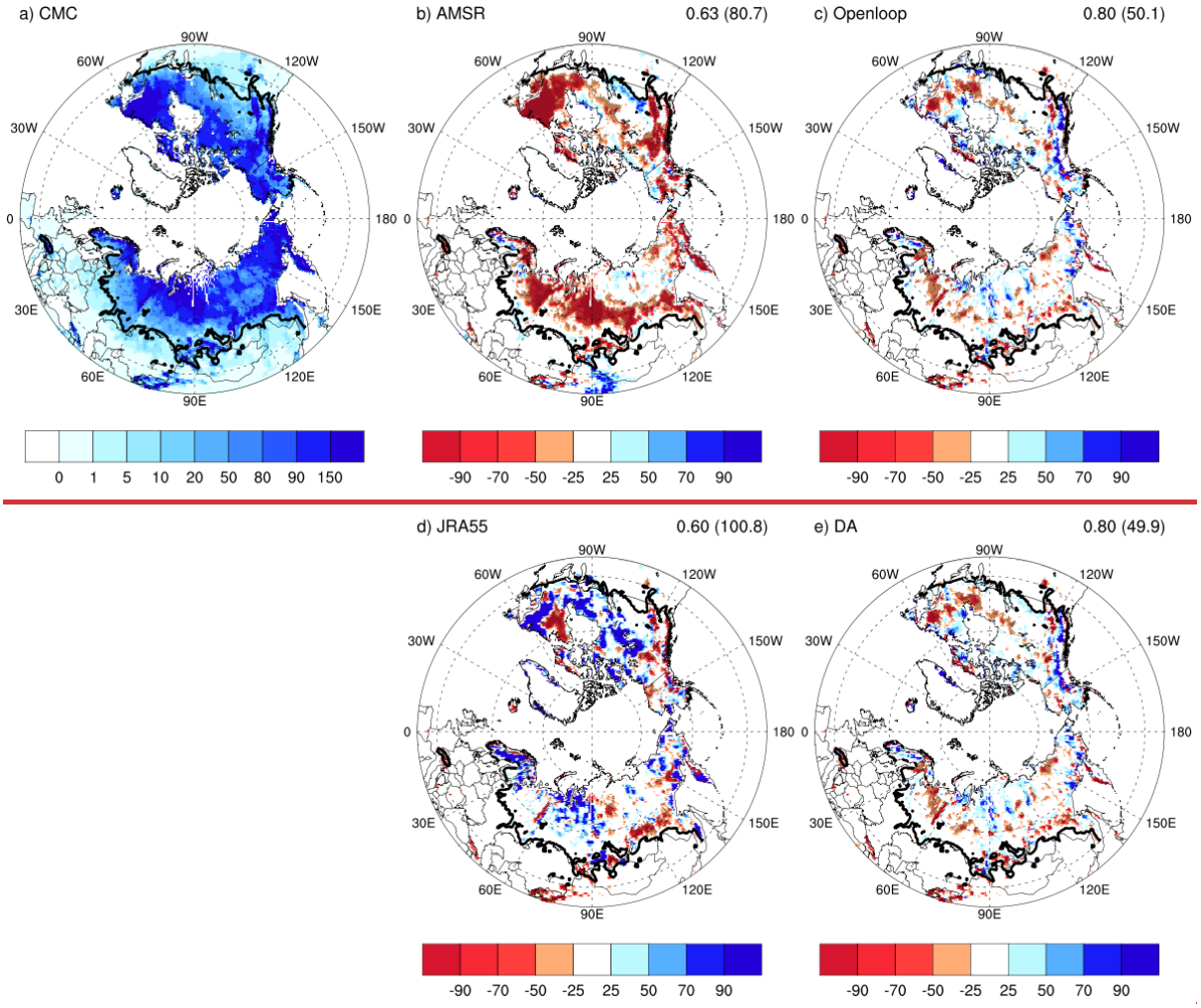
a) CMC
b) AMSR
0.63 (80.7)
c) Openloop
0.80 (50.1)
d) JRA55
0.60 (100.8)
e) DA
0.80 (49.9)
90W
60W
120W
30W
150W
0
180
30E
150E
60E
120E
90E
0 1 5 10 20 50 80 90 150
-90 -70 -50 -25 25 50 70 90

837

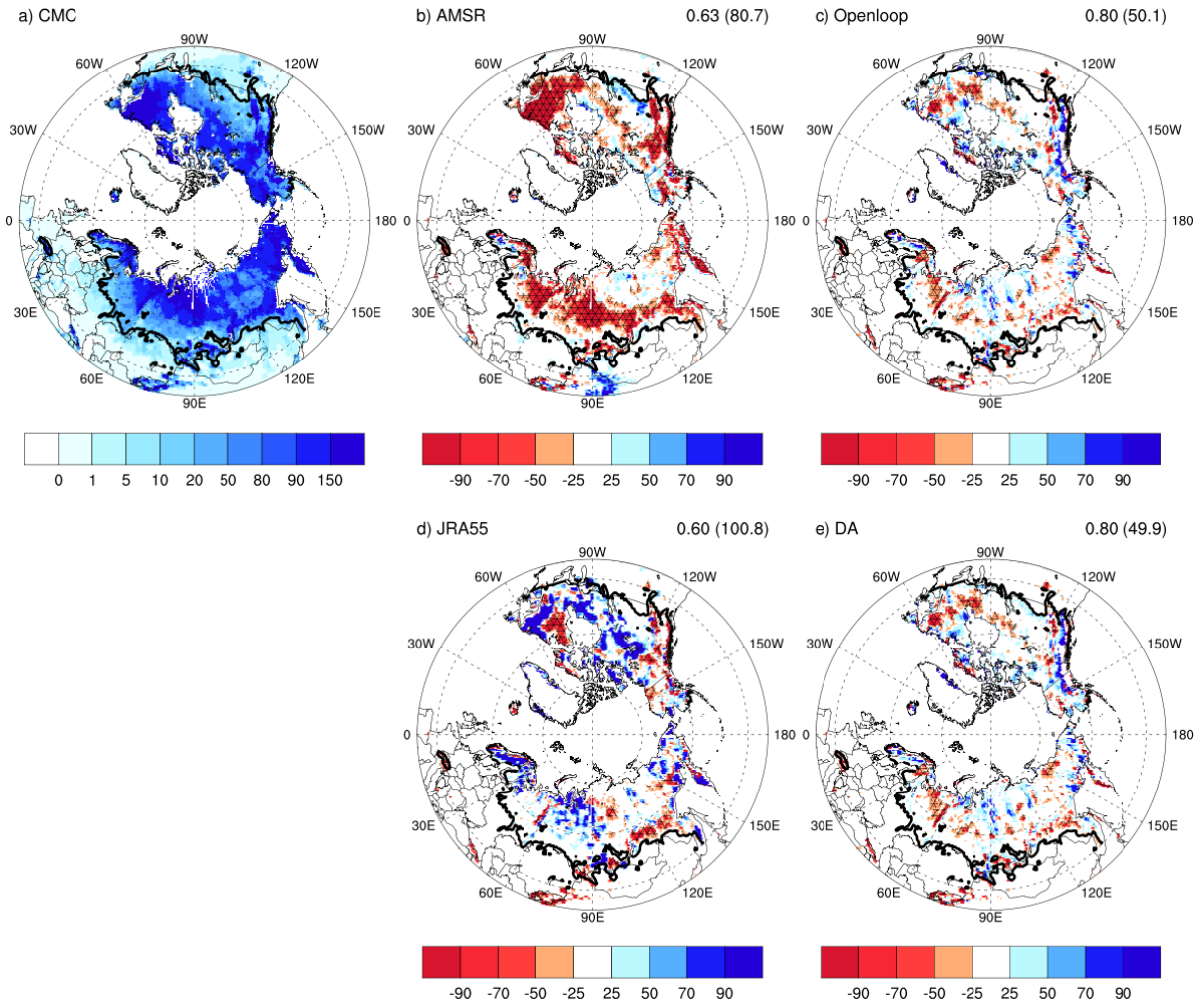

838

839 **Figure 3.** (a) Climatology of SWE (unit: kg/m^2 or mm), from CMC used as reference and (b-
840 e) the differences from CMC for AMSR2, base-line model simulation (Openloop),
841 JRA55, and the data assimilation results (DA) for April during 2013-2020. The black
842 line represents the boundary of the transition region, defined as the climatological-mean
843 SWE of less than 16mm. Each value on the top right is the pattern correlation with
844 CMC for 26482 pixels over 40 ºN and the root-mean-squared difference (unit: kg/m^2
845 or mm) from CMC (parenthesis) for 15323 pixels over 40-60ºN. Negative values (areas)
846 in red shades are indicated with ~~a diagonal line~~hatching.

847

848

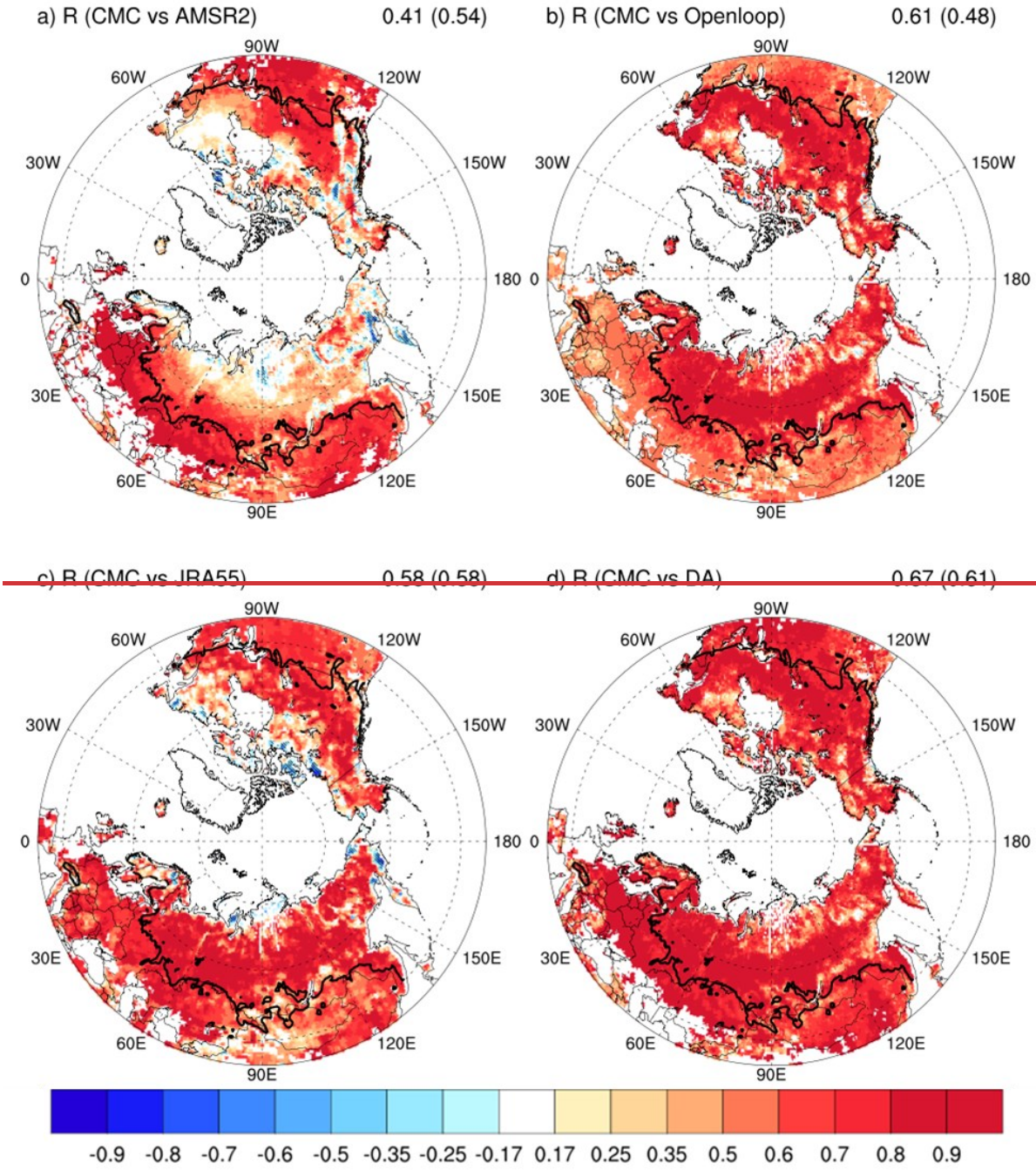
a) R (CMC vs AMSR2) 0.41 (0.54)
b) R (CMC vs Openloop) 0.61 (0.48)
c) R (CMC vs JRA55) 0.58 (0.58)
d) R (CMC vs DA) 0.67 (0.61)
90W
60W
120W
30W
150W
0
180
30E
150E
60E
120E
90E
-0.9 -0.8 -0.7 -0.6 -0.5 -0.35 -0.25 -0.17 0.17 0.25 0.35 0.5 0.6 0.7 0.8 0.9

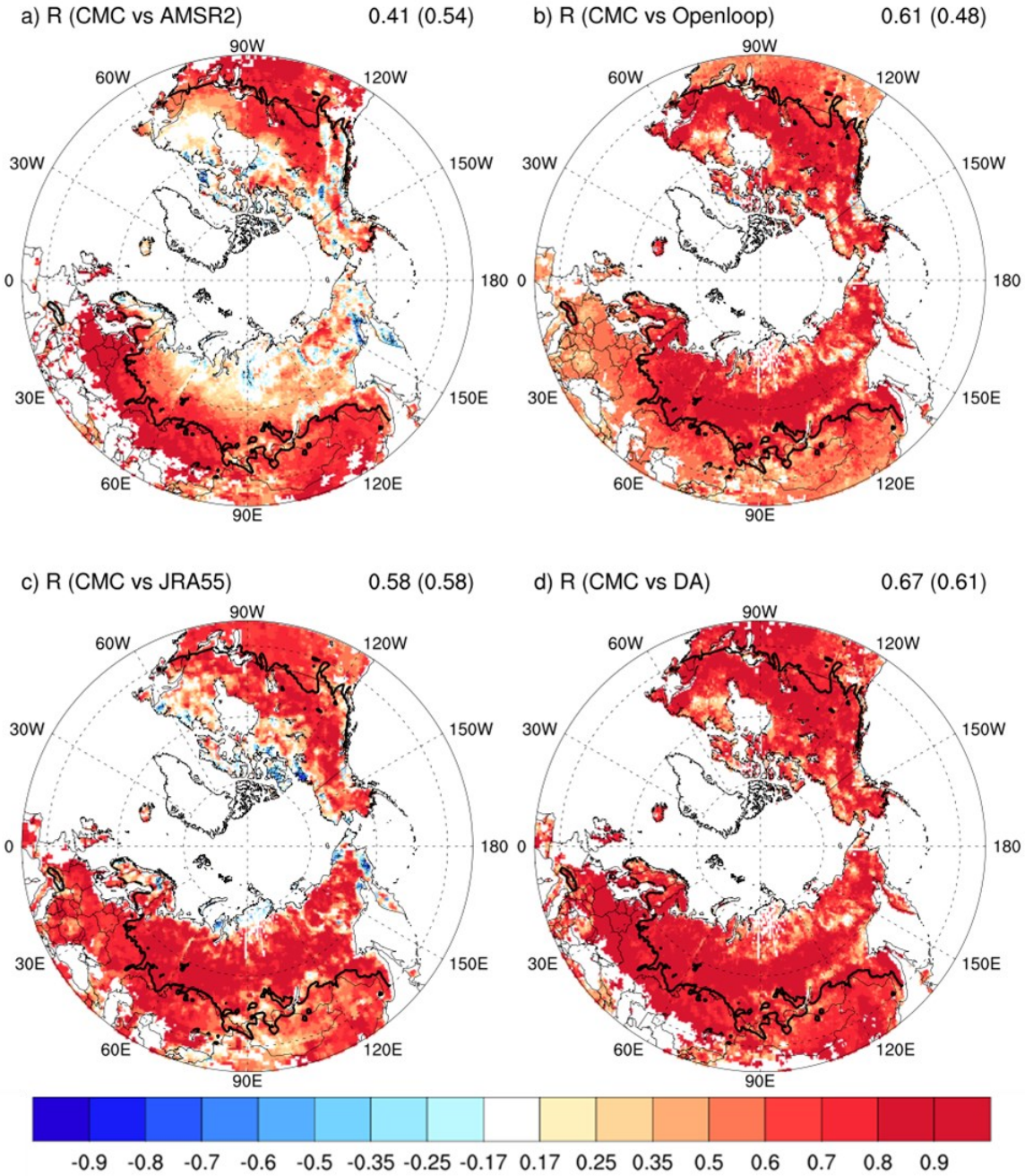

Figure 4. SWE skill measured as the Spearman rank correlation (R) with the CMC for AMSR2, base-line model simulation (Openloop), JRA55, and the data assimilation result (DA). The black line represents the boundary of the transition region, defined as the climatological-mean SWE of less than 16mm. Each value on the top is the area-average R of North hemisphere for 26482 pixels over 40°N and for 8801 pixels over the transition region (parenthesis). Negative values (areas) in red shades are indicated with ~~a diagonal line~~hatching.

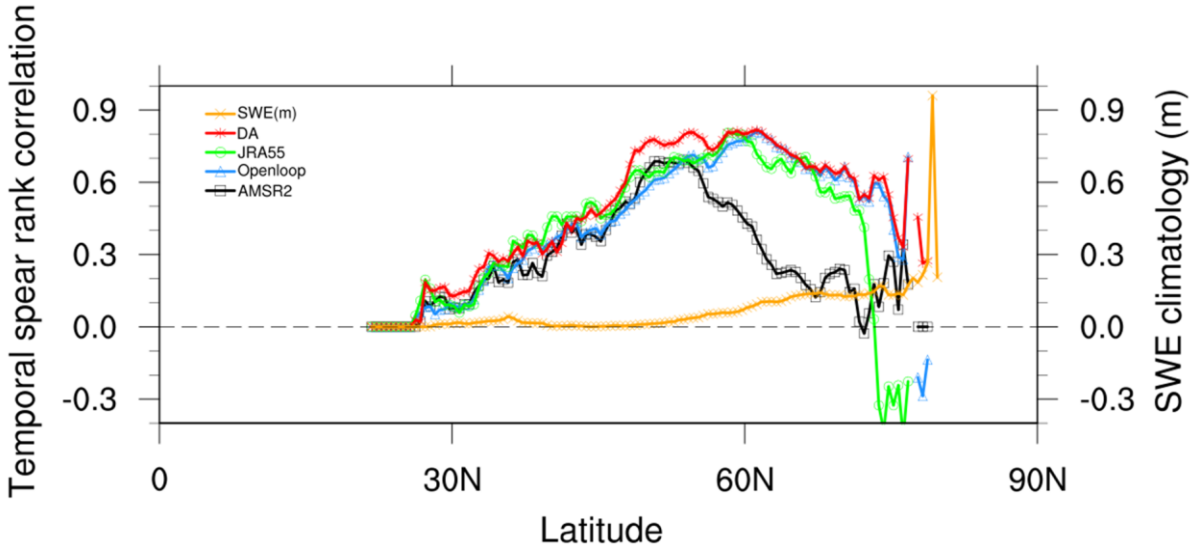

Figure 5. Zonally-averaged Spearman rank correlation (R) along the latitude for SWE. The yellow line indicates the climatology of SWE, and the black, blue, green, and red lines denote the values of AMSR2, base-line model simulation (Openloop), JRA55, data assimilation results (DA), respectively.

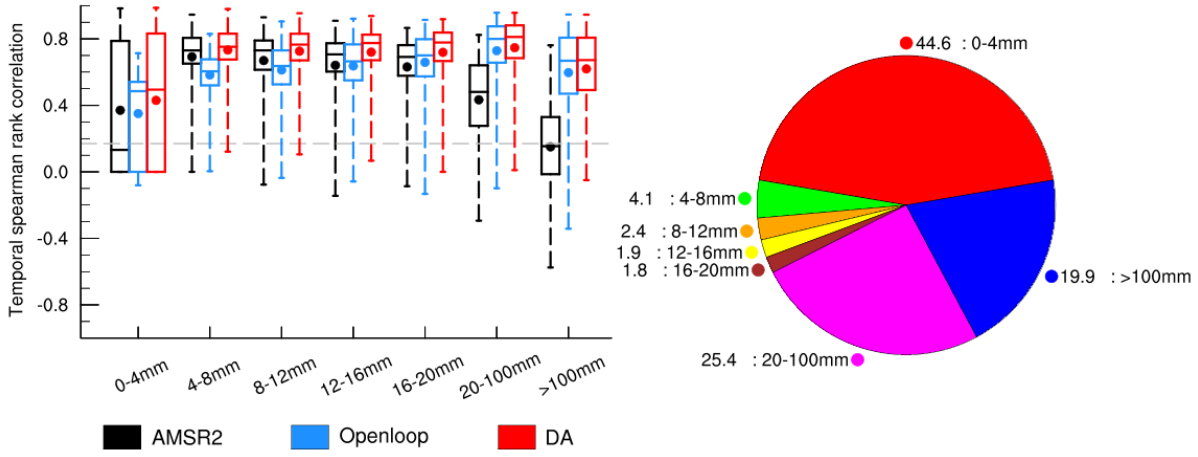

865

866 **Figure 6**. Box plots of the Spearman rank correlation (R) according to SWE~~.~~ (unit: kg/m^2 or
867 mm). The pie chart shows the total area ratio (%) as a function of SWE amount. The
868 black, blue, and red boxes denote the AMSR2, base-line model simulation (Openloop),
869 and the data assimilation results (DA), respectively. The boxes indicate 25 and 75%
870 percentiles, and the line and point in the boxes shows the median and the mean values.
871 The upper and lower whiskers denote the 10 and 90% percentiles, respectively.

872

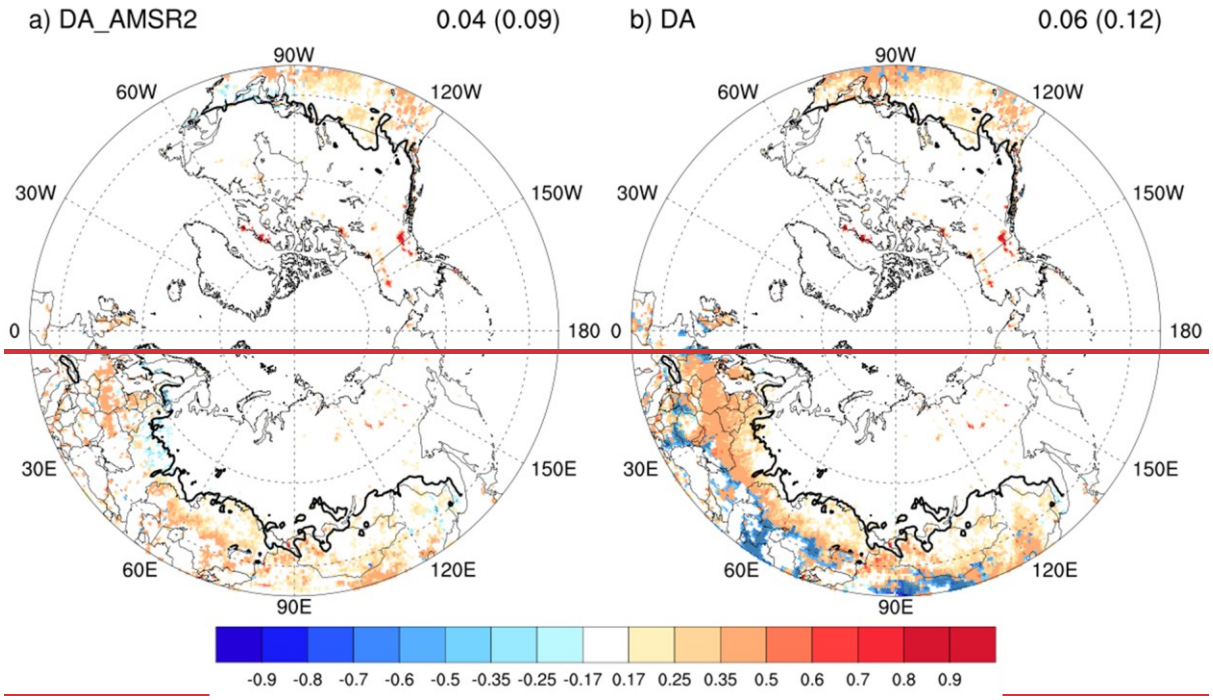

873

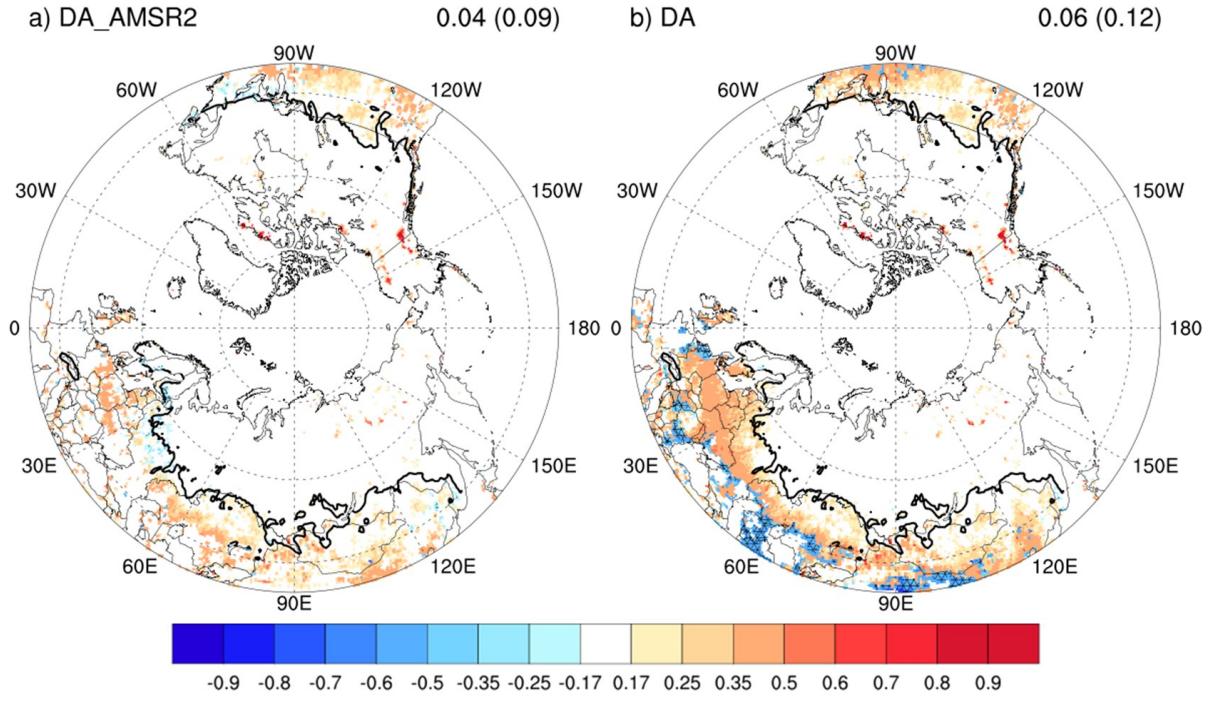

874

875 **Figure 7.** The difference in SWE Spearman rank correlation coefficient with CMC between
876 the Openloop and data assimilation results: DA employing both AMSR2 and IMS and
877 DA_AMSR2 utilizing solely AMSR2 and excluding IMS, for April during 2013-2020.
878 The black line represents the boundary of the transition region, defined as the
879 climatological-mean SWE of less than 16mm. Each value on the top right is the area-

880 average over 40ºN and the transition region (parenthesis). Negative values (areas) in
881 red shades are indicated with ~~a diagonal line~~hatching.
882
883
884

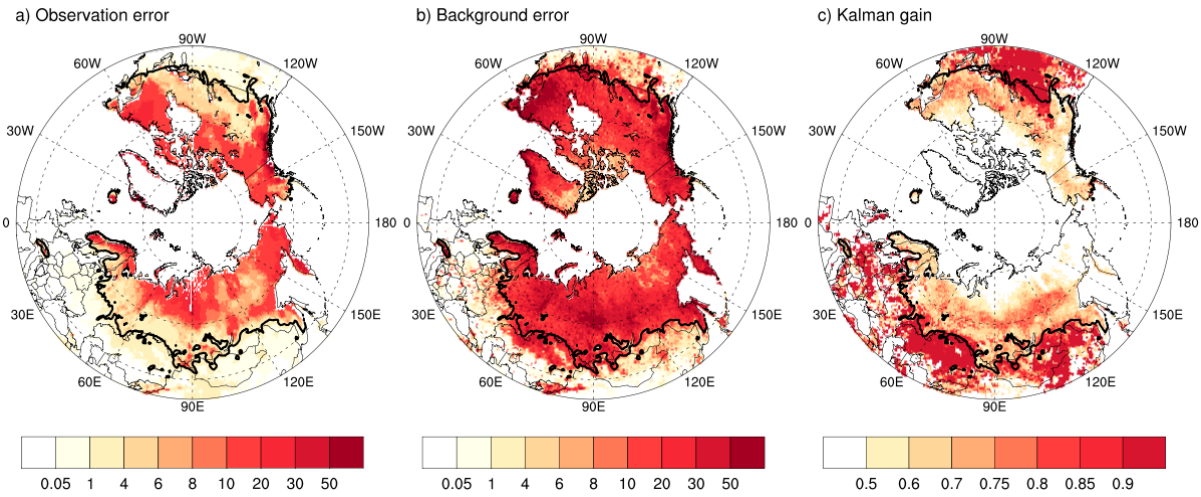

885

886 **Figure 8**. Spatial distribution of observation error (unit: kg/m^2 or mm), background error (unit:
887 kg/m^2 or mm), and Kalman gain. The black line represents the boundary of the
888 transition region, defined as the climatological-mean SWE of less than 16mm.

889

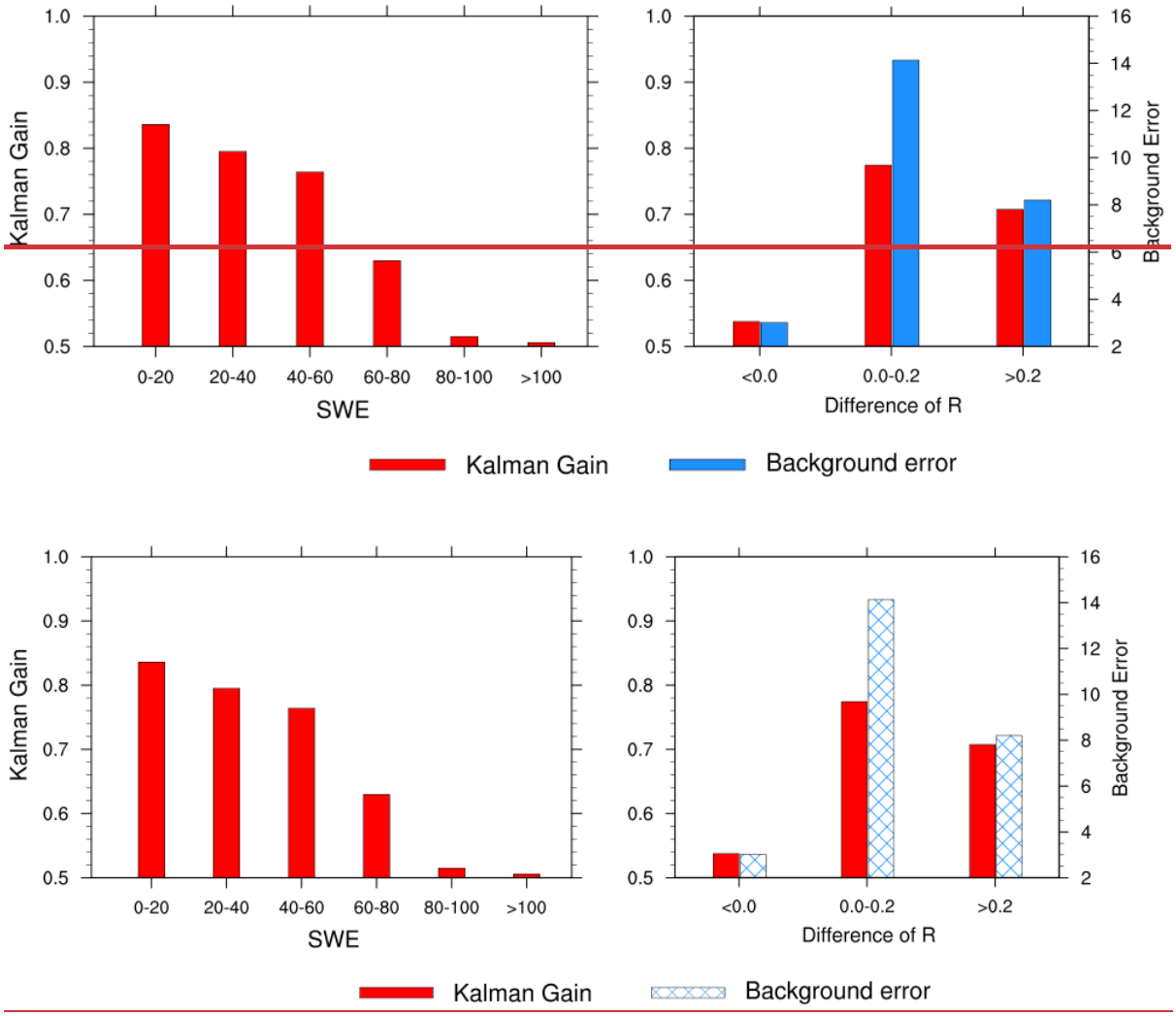

Figure 9. Bar chart of (left) the Kalman gain according to the SWE amount~~,~~ (unit: kg/m^2 or mm) and (right) the Kalman gain (red line) and background error (blue hatched line) as a function of the difference between Openloop and DA in Spearman rank correlation coefficient (R).

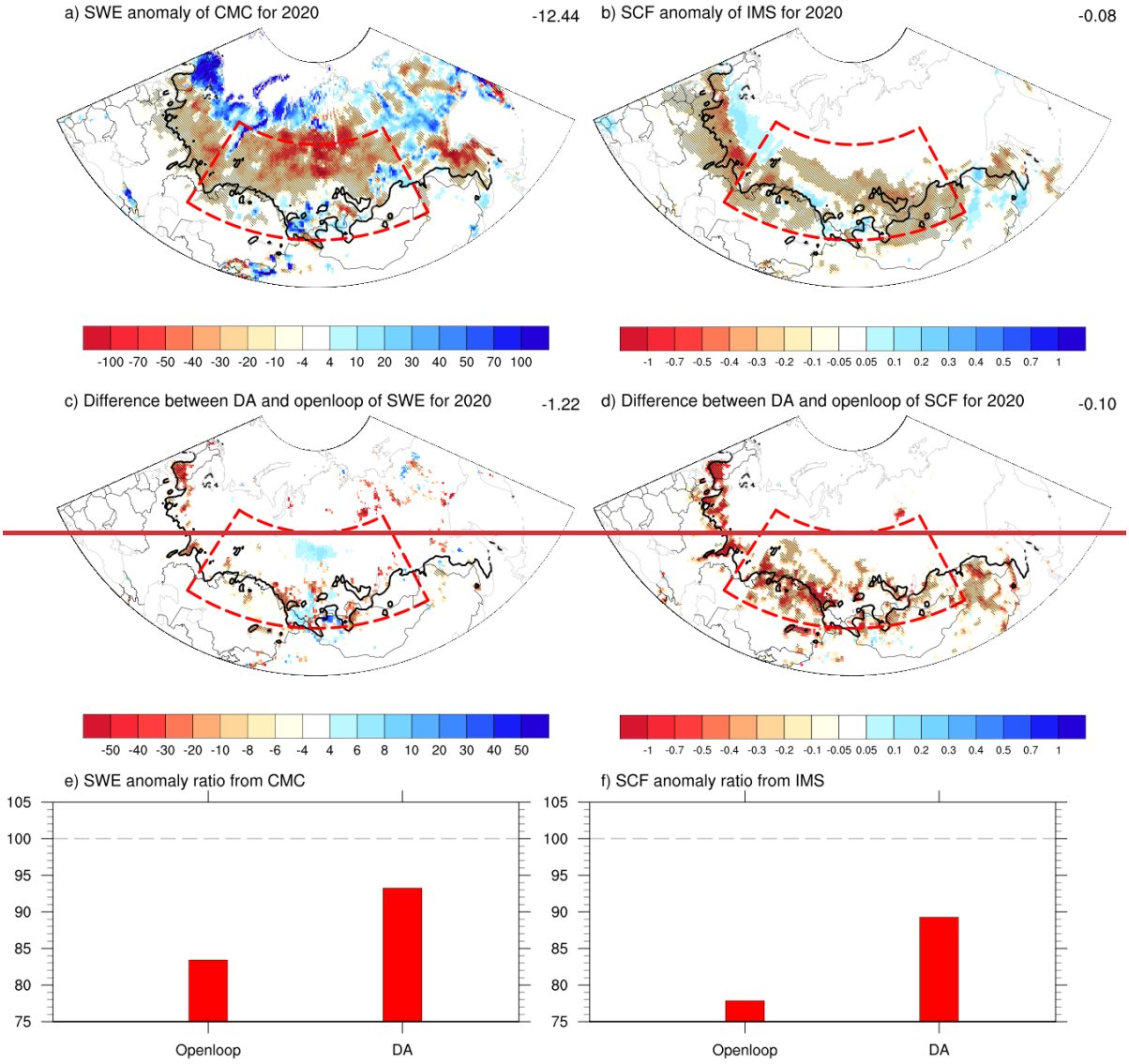
a) SWE anomaly of CMC for 2020
-12.44
b) SCF anomaly of IMS for 2020
-0.08
-100 -70 -50 -40 -30 -20 -10 -4 4 10 20 30 40 50 70 100
-1 -0.7 -0.5 -0.4 -0.3 -0.2 -0.1 -0.05 0.05 0.1 0.2 0.3 0.4 0.5 0.7 1
c) Difference between DA and openloop of SWE for 2020
-1.22
d) Difference between DA and openloop of SCF for 2020
-0.10
-50 -40 -30 -20 -10 -8 -6 -4 4 6 8 10 20 30 40 50
-1 -0.7 -0.5 -0.4 -0.3 -0.2 -0.1 -0.05 0.05 0.1 0.2 0.3 0.4 0.5 0.7 1
e) SWE anomaly ratio from CMC
f) SCF anomaly ratio from IMS
105
100
95
90
85
80
75
Openloop
DA

897

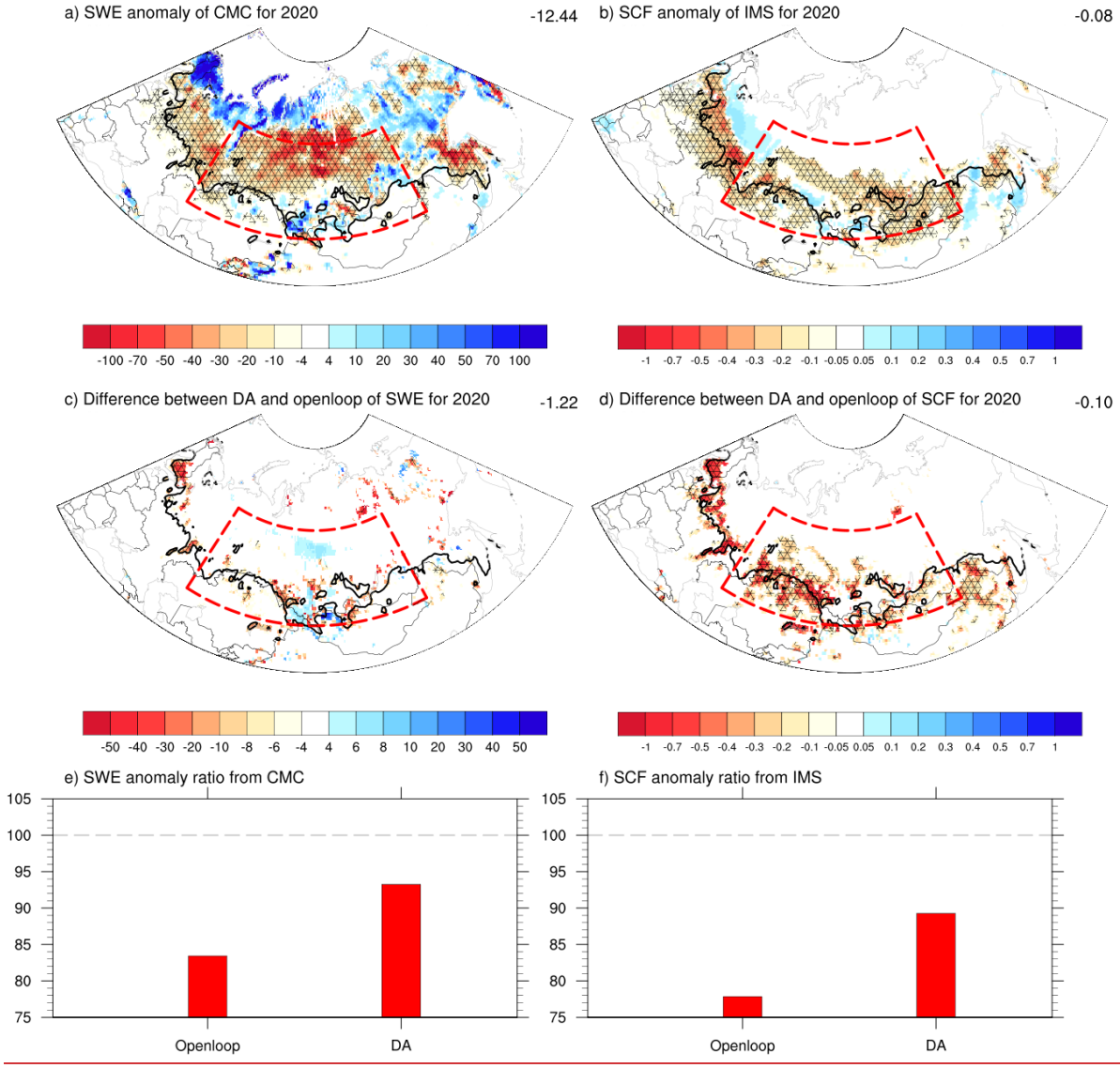

Figure 10. Anomalies of a) SWE (unit: kg/m^2 or mm) from CMC and b) SCF from IMS as well as the difference (c, d) of variables between DA and ~~openloop~~Openloop in April 2020. Bar chart (e, f) indicates the ratio of DA and ~~openloop~~Openloop to verification data such as CMC and IMS in the red box (48–65°N and 55–120°E), which is the region associated with extreme high-temperature events, focused on this study. Negative values (areas) in red shades are indicated with ~~a diagonal line~~hatching.